**University of South Florida**
**Scholar Commons**

Graduate Theses and Dissertations                                    Graduate School

September 2015

# A Study on 2.45 GHz Bandpass Filters Fabricated With Additive Manufacturing

Nicholas Christian Arnal
*University of South Florida*, arnaln@mail.usf.edu

A Study on 2.45 GHz Bandpass Filters

Fabricated With Additive Manufacturing


by


Nicholas C. Arnal


A thesis submitted in partial fulfillment
of the requirements for the degree of
Master of Science in Electrical Engineering
Department of Electrical Engineering
College of Engineering
University of South Florida


Major Professor: Thomas M. Weller, Ph.D.
Gokhan Mumcu, Ph.D.
Stephen E. Saddow, Ph.D.


Date of Approval:
April 27, 2015


Keywords: 3D printing, microwave filter, fused deposition modeling,
direct print additive manufacturing, square open loop resonator

**Dedication**


To my wife and best friend, Kathleen, who encourages me to be the best man I can be while

loving me unconditionally through the process.

To my parents, who have blessed me with abundant opportunity and support.

## Acknowledgments

I am pleased to extend my deepest gratitude to Dr. Thomas Weller, who has been an inspiring example of both hard and smart work as well as an excellent leader to work under. In addition, I would like to thank Dr. Gokhan Mumcu and Dr. Stephen Saddow for volunteering their time to be on my committee. I am extremely grateful for the help I received from Eduardo Rojas, Casey Perkowski, Sam Leblanc, and John Stratton – the work in this thesis would not have been done without them. I would like to thank Thomas Ketterl and Jon O'Brien for their help with HFSS. I would like to thank the Air Force, Sciperio, Jabil Circuit, Optomec, Modelithics and LPKF for their project sponsorship and/or support. The work in Chapter 4 was supported by USAF/AMFC under contract #FA8650-14-C-2421. Last but not least, I would like to thank the NREC Center at USF and the Florida High Tech Corridor for providing the tools and resources necessary to complete the work presented in this thesis.

# Table of Contents

# List of Tables

## List of Figures

iv

## Abstract

Square open loop resonator (SOLR) bandpass filters fabricated with additive manufacturing techniques are presented and studied. One filter contains novel 3D capacitive plates used to enhance resonator coupling. The filters are centered at 2.45 GHz and loaded with capacitors for miniaturization as low as 21% that of a conventional SOLR bandpass filter. The pass-band insertion loss of the filters ranges from 3.8 dB to 5.5 dB and the 3 dB bandwidth ranges from 180 MHz to 250 MHz. Also, degradation in the effective conductivity of printed ink as a function of substrate roughness is analyzed. Finally, a study of dielectric and metallic 3D printing processes that are candidates for digital manufacturing of integrated mobile phone client antennas is presented.

**Chapter 1: Introduction**

In recent years, substantial excitement has developed around additive manufacturing. With desktop printers available to the average consumer for less than $1000 [1], the general public has taken attention to 3D printing. Not only is the general public interested, but numerous large companies are using 3D printing such as Nike, General Electric, and Boeing [2]. There are many different applications for 3D printing including rapid prototyping, customized medical devices [3], unique limited run parts [4], and printed electronics. The work of this thesis is focused on the latter – and more specifically, the use of additive manufacturing in printing passive circuitry for high frequency applications.

Significant research is being done in the area of 3D printed electronics [5]-[7]. Electronics connected by printed lines are being embedded in 3D printed structures [8]-[10]. Numerous antennas for high frequency applications have been fabricated using additive manufacturing and inkjet printing [11]-[16]. Switched-line phase shifters [17], distributed impedance elements [18]-[19], and transmission lines [20] have also been fabricated using additive manufacturing.

A strong advantage of using additive manufacturing to print RF circuitry is the option to miniaturize in 3D. 3D miniaturization techniques, such as the folding and stacking methods shown in Figure 1.1, can be implemented with additive manufacturing. In addition to miniaturization, circuits can be printed to conform to a structure as shown in Figure 1.2.

www.manaraa.com
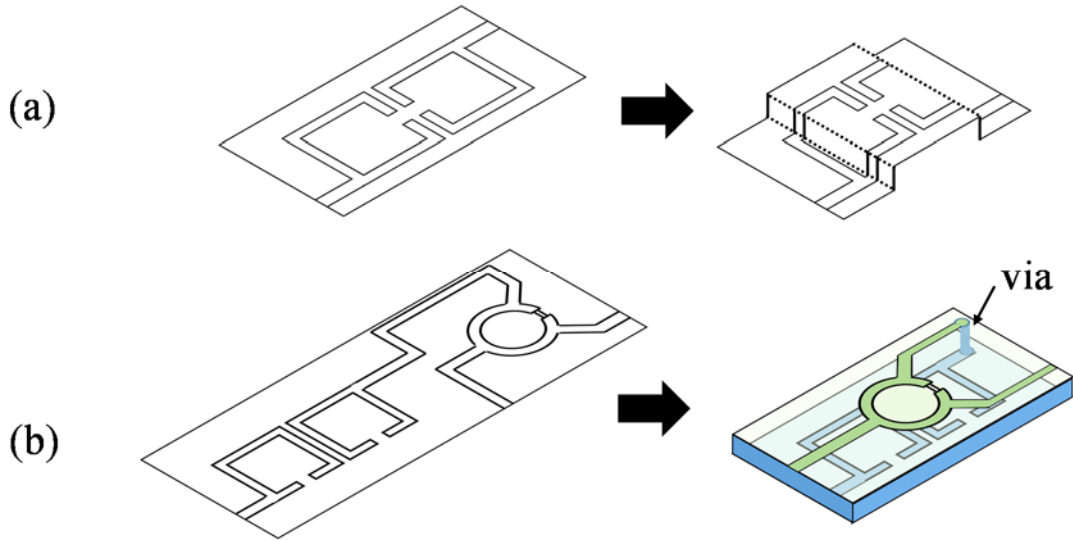
Figure 1.1 Possible 3D miniaturization by (a) folding and (b) stacking layers
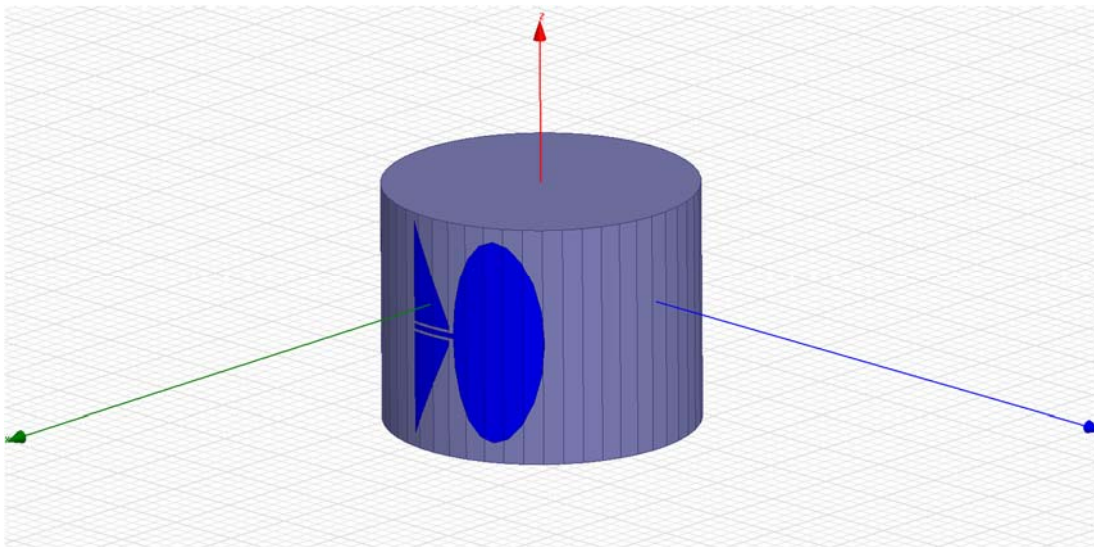


Figure 1.2 Antenna wrapped around cylinder

Currently, there are many areas in additive manufacturing that present challenges for RF circuitry. One issue is surface roughness. Certain printing processes, such as Fused Deposition Modeling (FDM), create parts with a surface roughness proportional to the size of the pen tip used for extrusion. Smooth surfaces are required for metallization because printed conductors conform to the surface of the part. A rough surface causes the effective conductivity of a printed

2

conductor to decrease and in the worst case, a discontinuity will occur. Another limitation is material selection. Currently, most substrates are printed with thermoplastics such as ABS, ULTEM, and polycarbonate via Fused Deposition Modeling. These thermoplastics have relative dielectric constants between 2-3 and loss tangents between 0.005-0.010. Obviously, these thermoplastics will not suffice if a higher dielectric constant is required.

At the present time, 3D printing is excellent for rapid prototyping low quantity parts, for creating 3D geometries that are not possible with conventional manufacturing processes, and for embedded design.

## 1.1 Thesis Overview and Contributions

The main goal of this thesis is to study high frequency circuits printed with additive manufacturing. Chapter 2 contains a brief overview of the prevalent printing processes for dielectric materials as well as conductors. Chapter 2 also contains a short summary of the common materials used for each printing process. Chapter 3 contains a theoretical background for the design of square open loop resonator (SOLR) bandpass filters. A practical design procedure based on the theory presented is given in Section 3.5. Chapter 4 contains the two major contributions of this thesis. The first contribution is the 3D printing of a miniaturized planar bandpass filter which has not been done before. The performance of the filter is comparable to the same filter fabricated on printed circuit board but the insertion loss is about 3 dB lower due to the effective conductivity of silver ink printed on a printed substrate. The second contribution is the design and 3D printing of a functional 3D bandpass filter using novel capacitive plates for coupling between the resonators. Chapter 5 concludes the thesis and

3

suggests recommendations for future work including improving the technology and future design ideas.

## Chapter 2: 3D Printing Background[1]

### 2.1 Introduction

There are numerous processes for additively manufacturing dielectric materials and conductive materials. There are multiple ways to classify the different printing processes [21], either by materials used, by baseline technology, or some combination of the two. One simple classification of the printing processes divides them by baseline technology into two categories. In all of the printing processes discussed below, besides Laser Direct Structuring, either material is extruded from a print head onto a substrate OR select areas of material lying in a liquid/powder bed are laser cured.

Printing processes for printing dielectric materials are discussed in Section 2.2. The included dielectric printing processes are Fused Deposition Modeling (FDM), PolyJet Printing, Selective Laser Sintering (SLS), and Stereolithography (SL). Section 2.2.5 contains surface roughness measurements for some of the processes. Processes for printing conductive materials are discussed in Section 2.3. The included conductor printing processes are Direct Print Additive Manufacturing (DPAM), Aerosol Jet Printing, and Laser Direct Structuring (LDS). Printable materials are discussed in Section 2.4.

---

[1] Portions of this chapter were previously published in [46]. Permission is included in Appendix A.

## 2.2 Dielectric Printing Processes

### 2.2.1 Fused Deposition Modeling (FDM)

Fused Deposition Modeling (FDM), shown in Figure 2.1, is a printing process where a thermoplastic is heated to a liquid state and deposited through a small pen tip. The plastic is heated just above its melting temperature and hardens almost immediately after deposition [21]. The part is built in layers from the bottom up. The print resolution is limited by the diameter of the hole in the extrusion head depositing the thermoplastic. For example, a high-end, commercially available printer has a minimum print resolution of 127 μm [22]. Others are pushing the limits down to 50 μm by using smaller pen tips [23]. A part printed with FDM is shown in Figure 2.2.

Since the material is deposited in lines and it hardens almost immediately upon deposition, peaks and valleys, like the ones shown in Figure 2.3, form along the surface of the part in the orientation of the build. Figure 2.4 displays the surfaces of three FDM prints. The surface roughness of an FDM print can be a limiting factor for certain applications, such as microwave circuits, where a smooth surface is required for high performance.
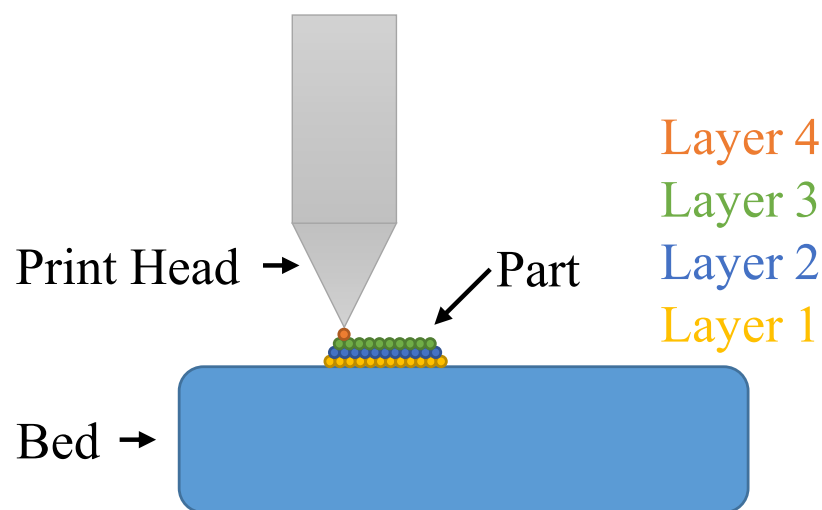


Figure 2.1 FDM printing process diagram

Figure 2.2 Polycarbonate phone cover with surface valleys printed via FDM
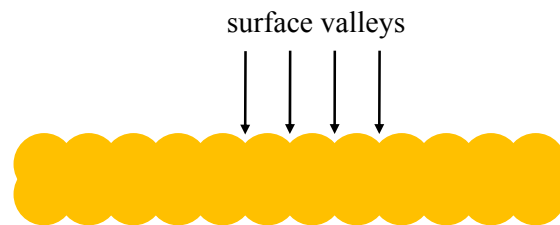
surface valleys



Figure 2.3 Diagram of surface valleys in FDM prints



Figure 2.4 Surfaces of FDM parts

### 2.2.2 PolyJet Printing

PolyJet printing, shown in Figure 2.5, uses inkjet technology to dispense UV-curable photopolymers onto a build tray. UV light cures the photopolymer almost immediately upon deposition. PolyJet is similar to FDM in that it deposits material but it differs in that it deposits a whole line of material drops at once instead of just one single drop. PolyJet print heads with multiple dispensers can print multiple materials at once [24]. The print resolution for a PolyJet part extends down to 16 μm due to the small droplets of material dispensed [25]. The high print resolution yields smooth surfaces like the ones shown in Figure 2.6.
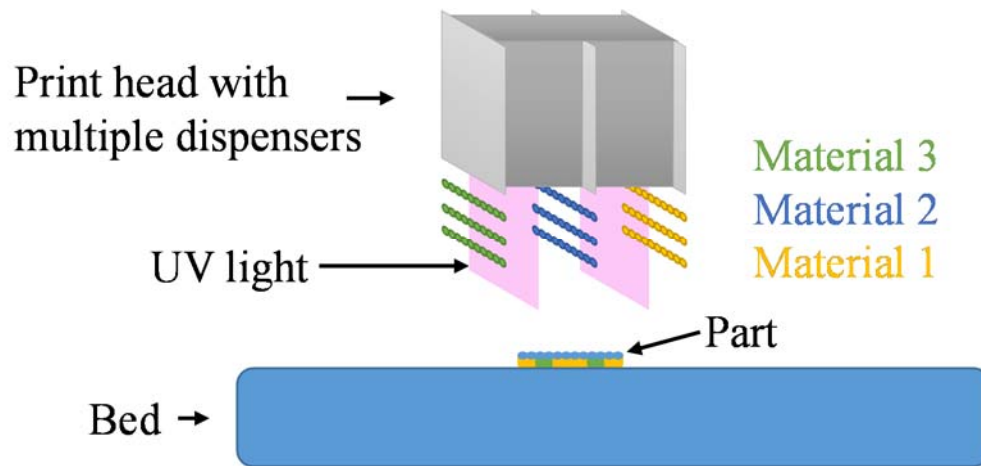


Figure 2.5 PolyJet printing process diagram
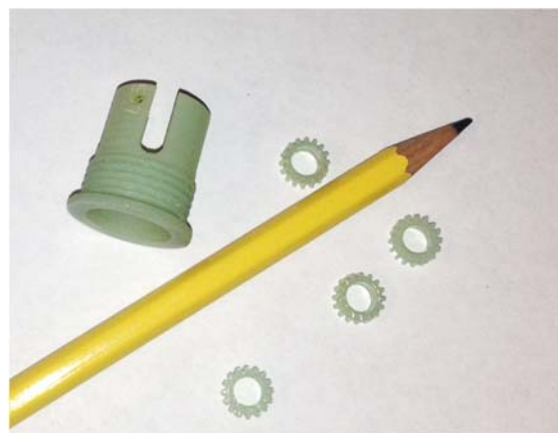


Figure 2.6 PolyJet printed parts

### 2.2.3 Selective Laser Sintering (SLS)

Selective Laser Sintering (SLS), shown in Figure 2.7, is a printing process where a part is created layer by layer with a laser that sinters powdered material sitting in a bed. After a layer is completed, the bed lowers, immersing the part in more powder so that the next layer can be laser sintered. SLS can be used to form nylon parts, metal parts, and glass parts [26]-[27]. A nylon SLS part is shown in Figure 2.8. SLS parts created from nylon powders have a sand-paper like finish which can be a problem for applications that require smooth surfaces.
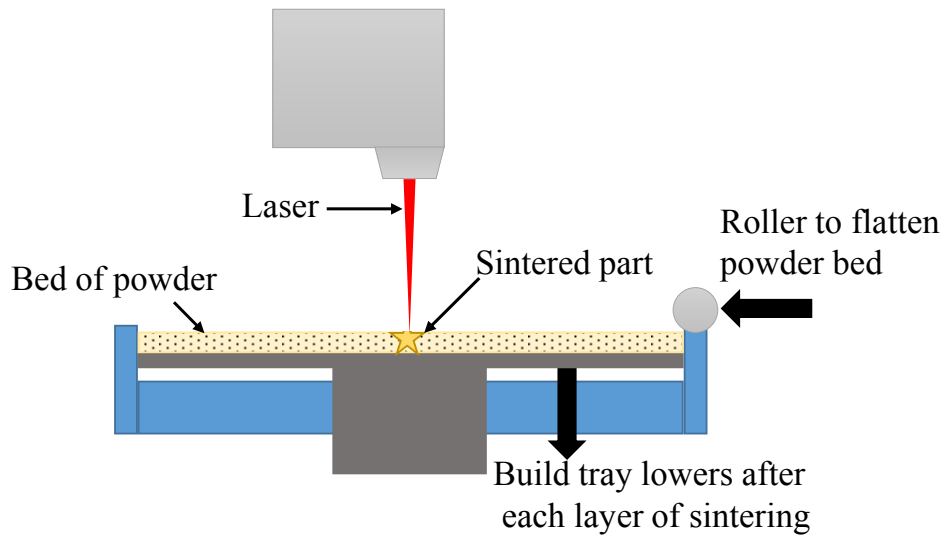
Figure 2.7 Selective Laser Sintering printing process diagram
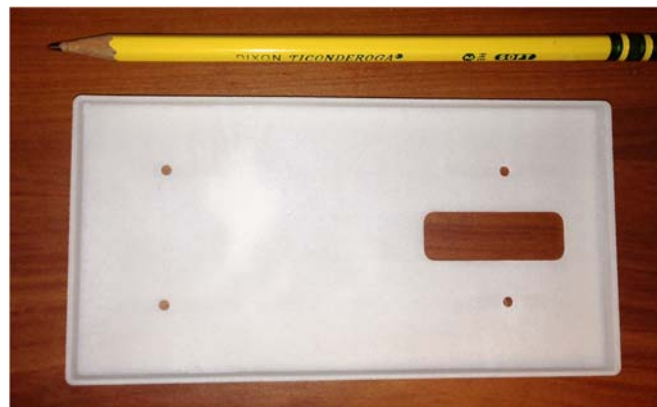
Figure 2.8 Duraform PA phone cover with sandpaper-like surface finish printed via Selective Laser Sintering

## 2.2.4 Stereolithography (SL)

Stereolithography (SL), shown in Figure 2.9, is a printing process where a part is created layer by layer with a laser that cures UV-curable, liquid resin sitting in a bed. After a layer is completed, the bed lowers and the part is immersed in more liquid resin so that the next layer can be cured. SL is very similar to SLS except it uses liquid resin instead of powder. The surface of an SL printed part, like the one in Figure 2.10, is very smooth because of the liquid resin.

UV light

Cured part

Bed of curable liquid resin

Build tray lowers after each layer of curing
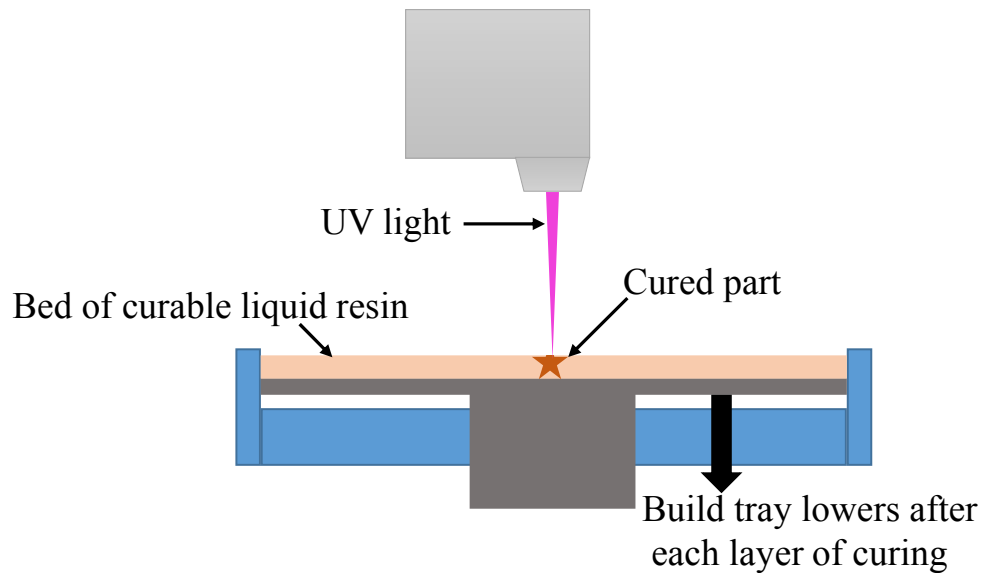
Figure 2.9 Stereolithography printing process diagram

Figure 2.10 Nanotool phone cover with smooth surface finish printed via Stereolithography

www.manaraa.com

## 2.2.5 Surface Roughness of Printed Dielectrics

A smooth surface is necessary for printing on because printed conductors conform to the surface of the part they are printed on. In Chapter 4, the effective RF conductivity is shown to decrease as the profile of the printed conductor becomes more non-uniform. All of the printing processes produce parts with different surface roughness values. The roughness value, $R_a$, describes the arithmetic average of peaks and valleys measured on a surface. Table 2.1 shows the measured $R_a$ values of identical parts produced by three dielectric printing processes – Fused Deposition Modeling (FDM), PolyJet printing, and Selective Laser Sintering (SLS). A disclaimer is necessary - the data in Table 2.1 is representative data and is only relevant to the samples generated for the project, not all samples generated by each printing process. The surface roughness of a printed part depends on the quality of the printer. The FDM sample is shown in Figure 2.11 for reference. The samples were measured in both the X and Y direction using a Dektak 150 Surface Profiler.

Table 2.1 Measured surface roughness values for FDM, PolyJet, and SLS parts

| Process | Material | $R_a$ (μm) | |
| --- | --- | --- | --- |
| | | X | Y |
| FDM | Polycarbonate | 7.15 | 7.29 |
| PolyJet | Digital ABS | 3.35 | 0.74 |
| SLS | Duraform PA | 13.37 | 11.31 |
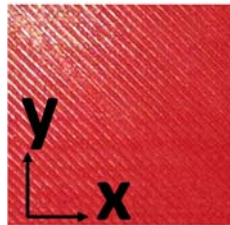


Figure 2.11 FDM sample used for surface roughness measurement

## 2.3 Conductor Printing Processes

### 2.3.1 Direct Print Additive Manufacturing (DPAM)

Direct Print Additive Manufacturing (DPAM), shown in Figure 2.12, is a printing process where ink is dispensed through a very small pen tip. Many pastes, including conductive ink, can be micro-dispensed with DPAM. The pen tip deposits pastes at a height of 50-100 μm above the surface of a substrate. Conductive ink needs to be cured at a higher temperature after printing.

The resolution of the print is dependent on the size of the pen tip used. The smallest pen tip currently available is 50 μm in diameter. 50 μm wide lines are the thinnest lines achievable with DPAM [28]. A smooth substrate surface is required for using DPAM in RF applications because the deposited ink conforms to the shape of the surface.
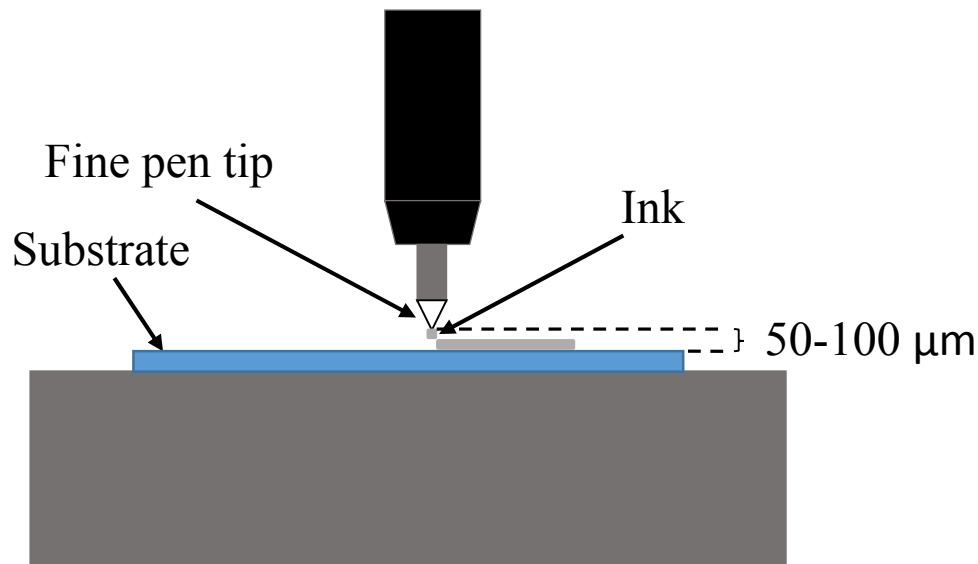
Figure 2.12 Direct Print Additive Manufacturing process diagram

### 2.3.2 Aerosol Jet Printing

In Aerosol Jet printing, nanoparticle inks are atomized and then sprayed onto a surface as shown in Figure 2.13. After printing, the part is heated for the removal of solvents and sintering of the metal. The resistivity of the printed particles decreases as the post printing sintering

temperature increases [29]. The feature resolution extends down to 10 μm for Aerosol Jet printing [30]. Just as in DPAM, a smooth substrate is required for using Aerosol Jet in RF applications because the sprayed nanoparticles conform to the shape of the surface.
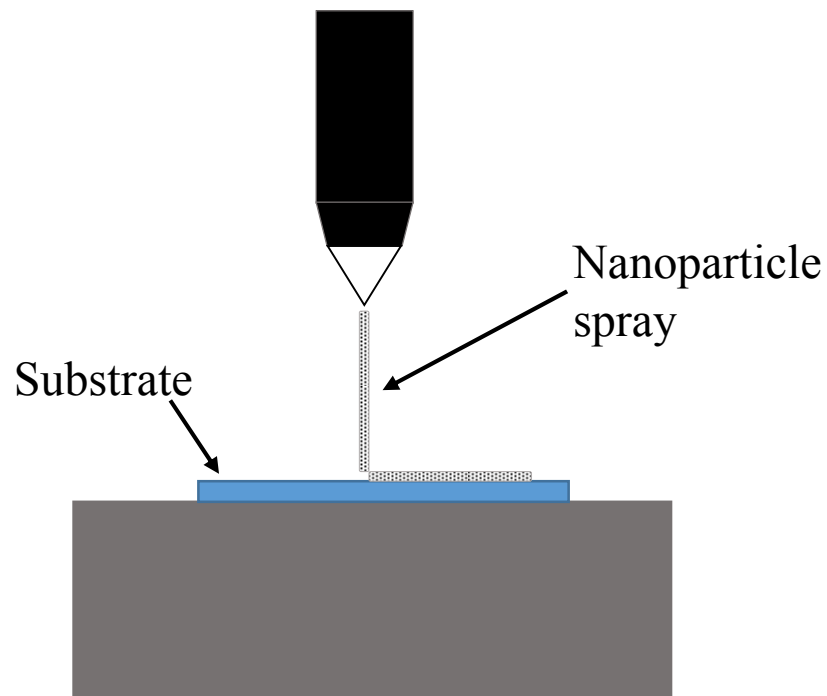


Figure 2.13 Aerosol Jet process diagram

### 2.3.3 Laser Direct Structuring (LDS)

Laser Direct Structuring (LDS), shown in Figure 2.14, is a process where a part contains an additive that is laser activated in select areas. The laser-activated area is fully metalized through copper plating. Other metals can be used such as nickel and gold. LDS is a process widely used in industry for circuits printed on complicated 3D geometries [31]. Although LDS is technically not a printing process, it is used for very similar applications.

13
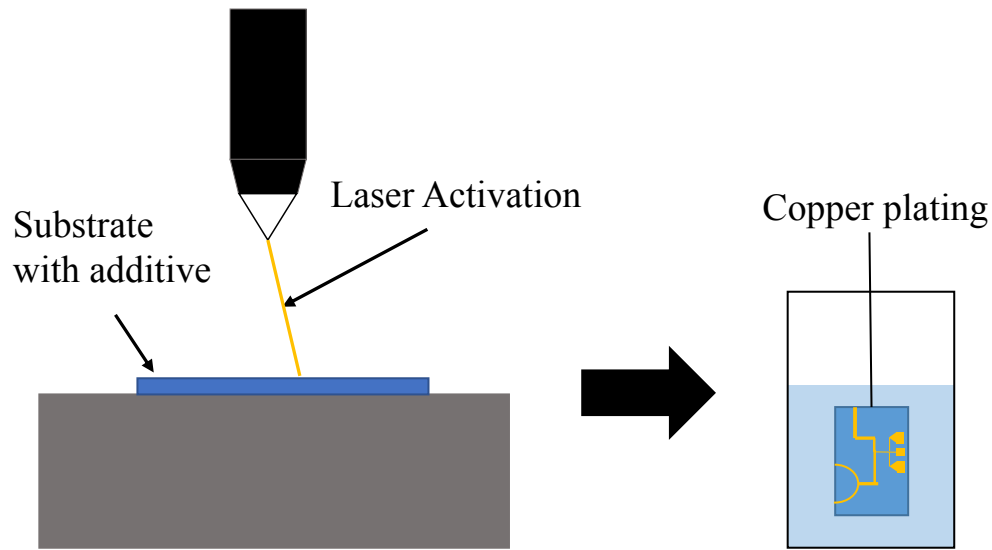
Figure 2.14 Laser Direct Structuring process diagram

## 2.4 Materials

### 2.4.1 Printable Dielectrics

A list of common dielectric materials used for 3D printing is given in Table 2.2 [46]. Among these commercially available dielectrics, Acrylonitrile Butadiene Styrene (ABS) is often a preferred material due to its good RF properties [32] and its smooth surface finish after treatment. Polycarbonate (PC), with similar electrical properties as ABS, is also commonly used and has long been a mainstay for injection-molded plastic applications, although for 3D printed structures surface smoothing processes are not as readily available as they are for ABS. A smooth surface is essential when 3D printing conductive materials with high resolution and line control. Nevertheless, for certain metallic printing processes a higher melting temperature is required which precludes the use of ABS; e.g., the aerosol jet method [33] requires dielectrics that melt above 120°C making PC a viable option. ULTEM, another thermoplastic used in fused deposition modeling (FDM), has a high melting temperature and RF properties similar to PC and

14

ABS. The so-called Digital ABS is by far the smoothest material to print with. However, the loss

tangent of this UV-cured material is significantly higher than those of the ABS and PC

thermoplastics. The heat deflection temperature (HDT) is also much lower than the

thermoplastics. Treatment processes to raise the HDT are available [34]. Duraform PA is a nylon

material in powder form that is used in sintering processes, like SLS. Duraform PA is not

preferable for RF applications because the loss tangent is twice as large as ABS and PC.

Table 2.2 Common dielectric materials. © 2015 IEEE

| Material | Process | Relative Dielectric Constant | Loss Tangent | HDT (°C) | Comments |
|---|---|---|---|---|---|
| Acrylonitrile butadiene (ABS) | FDM | 2.3-2.8 | 0.006 | 96 | Low loss tangent. Smoothing available. |
| Polycarbonate (PC) | FDM | 2.5 | 0.005 | 138 | Low loss tangent. |
| Digital ABS | PolyJet | 3.1 | 0.044 | 58-100 | Smooth surface with great feature resolution. High loss tangent. Low HDT. |
| Duraform PA ® | SLS | 2.4 | 0.011 | 180 | High loss tangent. |

**2.4.2 Printable Conductors**

There are two common options for additively manufactured conductive materials. The

first option is metallic, typically silver, nanoparticle inks which are often deposited by spraying

(e.g. with an ink-jet printer) or screen printing. The resulting thin film layers can be oven cured,

or by using high intensity optical systems that are convenient when low temperature substrates

are used. The DC conductivity of silver deposited using aerosol jet printing is, at best, 1/7 of the

15

bulk conductivity of bulk silver [35]. The conductivity degrades as the sintering temperature decreases [29]. The second common option is a conductive paste, such as Dupont CB028, a silver paste that is used with dispensing systems and thermally cured at 90-160°C. The DC conductivity of CB028 is on the order of 1/10 that of bulk silver.

16

## Chapter 3: Square Open Loop Resonator (SOLR) Bandpass Filter Background

### 3.1 Introduction

In today's wireless industry, compact and cost-effective filters are highly desirable. Planar filters are preferable as they can be fabricated using printed-circuit technology [36]. Research is being done in the miniaturization of coupled resonator bandpass filters made using microstrip [37]-[40]. Square open loop resonator bandpass filters are small in size ($\lambda$/8 x $\lambda$/8) and can be further miniaturized with meandered lines [36] and capacitive loading [37].

Some key properties of open circuited $\lambda$/2 microstrip resonators, such as input impedance and quality factor, are examined in Section 3.2. The external quality factor of square open loop resonators is discussed in Section 3.3 and a measurement technique is presented. Coupling methods between resonators is discussed in Section 3.4 and a measurement technique is presented. A design procedure for SOLR bandpass filters is given in Section 3.5. Lastly, a specific method of miniaturization utilizing surface mount capacitors is briefly discussed in Section 3.6.

### 3.2 Open Circuited $\lambda$/2 Resonators

An open circuited microstrip line like the one shown in Figure 3.1 behaves as a resonator when the length, $l$, is an integer multiple of $\lambda$/2 [41]. The input impedance is given as

$$Z_{IN} = Z_0 \frac{1 + j \tan(\beta l) \tanh(\alpha l)}{\tanh(\alpha l) + j \tan(\beta l)}. \tag{3.1}$$

17

Nearby the resonant frequency, where $\omega = \omega_0 + \Delta\omega$ and $l = \frac{\lambda_0}{2}$,

$$\beta l = \frac{2\pi}{\lambda}\frac{\lambda_0}{2} = \frac{\pi\lambda_0}{\frac{2\pi c}{\omega}} = \frac{\lambda_0(\omega_0 + \Delta\omega)}{2c} = \frac{2\pi(\omega_0 + \Delta\omega)}{2\omega_0} = \pi + \pi\frac{\Delta\omega}{\omega_0}. \quad (3.2)$$

The following simplifications can be made to the trigonometric functions in Equation 3.2 near the resonant frequency:

$$\tan(\beta l) = \tan\left(\pi + \pi\frac{\Delta\omega}{\omega_0}\right) \approx \pi\frac{\Delta\omega}{\omega_0} \quad (3.3a)$$

$$\tanh(\alpha l) \approx \alpha l \quad (3.3b)$$

Plugging Equations 3.3a and 3.3b into Equation 3.1 and simplifying leads to

$$Z_{IN} = \frac{Z_0}{\alpha l + j\left(\pi\frac{\Delta\omega}{\omega_0}\right)} \quad (3.4a)$$

or after dividing by $\alpha l$,

$$Z_{IN} = \frac{\frac{Z_0}{\alpha l}}{1 + j\left(\frac{\pi}{\alpha l}\frac{\Delta\omega}{\omega_0}\right)}. \quad (3.4b)$$

Equation 3.4b is in the same form as the equation for the input impedance of a parallel RLC resonator near resonance with a quality factor of $Q_0$, which is given as

$$Z_{IN} = \frac{R}{1 + j2\Delta\omega RC}. \quad (3.5)$$

Using Equations 3.4b and 3.5, the equivalent RLC values for an open circuited $\lambda/2$ microstrip resonator be expressed as

$$R = \frac{Z_0}{\alpha l} \quad (3.6a)$$

$$C = \frac{\pi}{2\omega_0 Z_0} \quad (3.6b)$$

18

$$L = \frac{1}{\omega_0{}^2 C} \qquad\qquad (3.6c)$$

with an internal quality factor of

$$Q_0 = \omega_0 RC = \frac{\pi}{2\alpha l} = \frac{\beta}{2\alpha}. \qquad\qquad (3.6d)$$
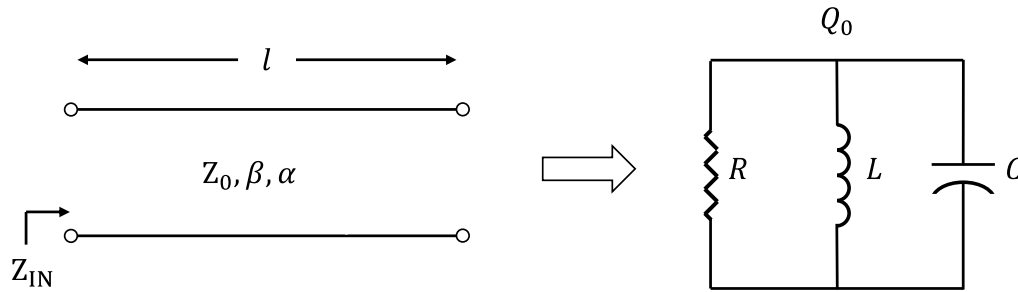


Figure 3.1 Open circuited microstrip line and its equivalent circuit at resonance

As seen in Equation 3.6d, a resonator's quality factor is inversely proportional to the attenuation constant of the material used. The quality factor approaches infinity as the attenuation constant approaches zero.

### 3.2.1 Square Open Loop Resonators

A common way to miniaturize an open circuited $\lambda/2$ resonator is to fold it into a square with a gap as shown in Figure 3.2 resulting in an approximate area of $\lambda/8$ x $\lambda/8$.
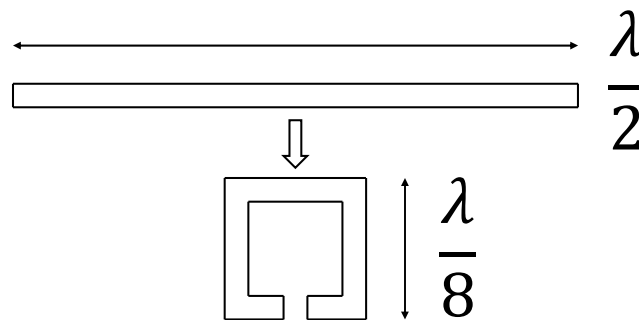


Figure 3.2 Square open loop resonator formation by the folding of an open circuited $\lambda/2$ resonator

19

### 3.3 External Quality Factor

A resonator must be tapped into with some feed line. The method in which the resonator is fed determines the external quality factor of the resonator, $Q_e$. $Q_e$ contributes to both the bandwidth and the insertion loss of the filter. A common way to feed a resonator is to feed it directly with a 50$\Omega$ feed line as shown in Figure 3.3. In Figure 3.3, $d_t$ represents the distance from the center of the resonator to the center of the feed line. The external quality factor of a single unloaded resonator with a resonant frequency of $f_c$ can be calculated by looking at the phase response of $S_{11}$ near resonance. Let $f_{c+}$ and $f_{c-}$ represent the frequencies at which the phase of $S_{11}$ is greater than or less than the phase at $f_c$ by 90° as shown in Figure 3.4. In equation form,

$$phase(S_{11})|_{f_{c\pm}} = phase(S_{11})\Big|_{f_c} \pm 90° \tag{3.7}$$

Once $f_{c+}$ and $f_{c-}$ are determined, $Q_e$ can be calculated directly using the following formula [42]:

$$Q_e = \frac{f_c}{|f_{c+} - f_{c-}|} \tag{3.8}$$

At $d_t = 0$, the feed line is tapping into a null in the electric field of the resonator making $Q_e$ a very large value. $Q_e$ decreases as $d_t$ increases and approaches half the total resonator length.
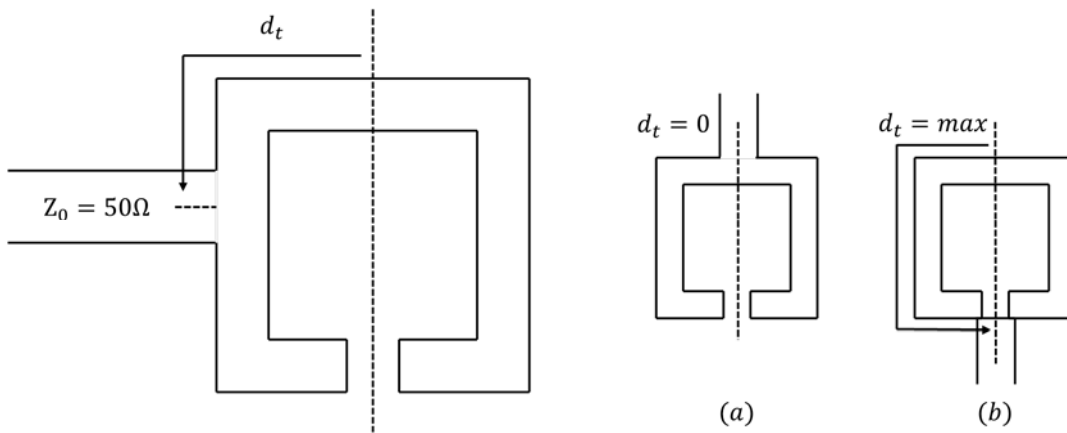


Figure 3.3 Feed line tapping into resonator at distance $d_t$. (a) $d_t = 0$ (b) $d_t =$ max

20
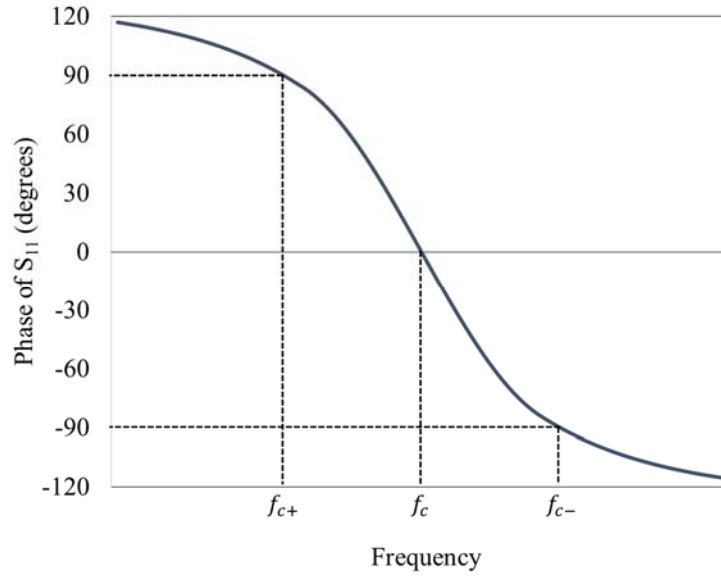
Figure 3.4 $S_{11}$ phase response showing $f_{c+}$ and $f_{c-}$

### 3.4 Coupled Resonators

Resonators can be coupled together via electromagnetic coupling [42]. The coupling coefficient, k, is a function of two sets of adjacent electric and magnetic fields, **H** and **E**. The coupling coefficient, *k,* is defined as the ratio of coupled energy to stored energy and is given by the following equation:

$$k = \frac{\iiint \varepsilon \mathbf{E_1} \cdot \mathbf{E_2} dv}{\sqrt{\iiint \varepsilon |\mathbf{E_1}|^2 dv \times \iiint \varepsilon |\mathbf{E_2}|^2 dv}} + \frac{\iiint \mu \mathbf{H_1} \cdot \mathbf{H_2} dv}{\sqrt{\iiint \mu |\mathbf{H_1}|^2 dv \times \iiint \mu |\mathbf{H_2}|^2 dv}} \quad (3.9)$$

Three coupling modes exist – electric coupling, magnetic coupling, and mixed coupling which consists of both electric and magnetic coupling. Electric coupling is accounted for by the first term in (3.9) while magnetic coupling is accounted for by the second term. The different coupling modes for square open loop resonators are shown in Figure 3.5**.** The coupling is a function of the gap between the resonators and stronger coupling is achieved as the gap is reduced.

21
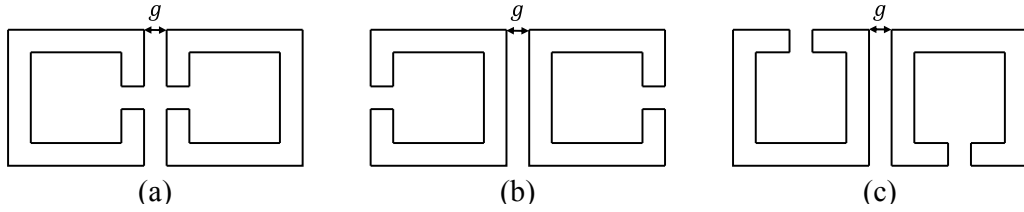
Figure 3.5 Electric coupling (a), magnetic coupling (b), and mixed coupling (c) modes for square open loop resonators.

The calculation of k requires that you know the electric and magnetic field vectors which is impractical in many situations. An alternative calculation of k utilizing the frequency response of the coupled resonators is derived in [42] using lumped-element circuit models. In summary, when two identical resonators with self-resonant frequencies at $f_c$ are coupled together, two distinct resonant frequencies, $f_H$ and $f_L$, are produced. The amount of either electric, magnetic, or both electric and magnetic coupling between the resonators impacts the spacing between $f_H$ and $f_L$. The greater the coupling coefficient k, the greater the difference in frequency between $f_H$ and $f_L$. The equation for k based on the resonant frequencies of the coupled resonators is as follows:

$$k = \frac{f_H{}^2 - f_L{}^2}{f_H{}^2 + f_L{}^2} \tag{3.10}$$

The resonant frequencies, $f_H$ and $f_L$, can be determined from a plot of $S_{21}$ versus frequency of the coupled resonators and then k can be calculated. As an example, the plot in Figure 3.6 shows the $S_{21}$ response of two coupled resonators. In the plot, $f_H$ and $f_L$ are at 2.668 GHz and 2.565 GHz respectively, which leads to a coupling coefficient of k = 0.0394.
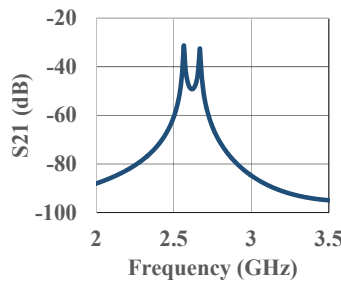


Figure 3.6 $S_{21}$ response of coupled resonators with coupling factor k=0.0394

22

### 3.5 SOLR Bandpass Filter Design Procedure

Coupled resonator bandpass filters can be designed starting with lowpass prototype filter values. For an $n^{th}$ order filter with $n$ resonators, $n+1$ prototype values $(g_0, g_1 \ldots g_{n+1})$ must be selected. The fractional bandwidth (FBW) of the filter must also be predetermined. With these values chosen, the following formulas can be used to calculate the external input and output quality factors, $Q_{ei}$ and $Q_{eo}$, as well as the coupling coefficients, $k_{ij}$, required between resonators $i$ and $i+1$ [42]:

$$Q_{ei} = \frac{g_1}{FBW} \tag{3.11}$$

$$Q_{eo} = \frac{g_n}{FBW} \tag{3.12}$$

$$k_{ij} = \frac{FBW}{\sqrt{g_i g_{i+1}}} \tag{3.13}$$

Once the external quality factors and coupling coefficients are known, a coupled square open loop resonator bandpass filter can be designed using the following procedure:

1. Design a resonator with a resonant frequency equal to the center frequency of the filter.

2. Determine the tap location, $d_t$, for both the input and output feed lines using the method described in Section 3b to achieve the desired external quality factors, $Q_{ei}$ and $Q_{eo}$.

3. Determine the gap distances required between adjacent resonators to achieve the coupling coefficients, $k_{i,i+1}$ by the method described in Section 3c.

4. Optimize the design as needed.

23

The low pass filter prototype values predict an ideal filter performance that does not account for losses in the ideal lumped components, or in this case, losses in the resonators themselves due to radiation, substrate, or conductive losses as well as dispersion and surface roughness [43]. Although the procedure neglects these losses, the pass band insertion loss of a coupled resonator filter ultimately is dependent on the internal quality factor of each resonator. With that being said, the design procedure is still valid for designing filters but the loss will be higher than predicted by the prototype elements depending on the make-up of the resonators.

### 3.6 Miniaturization via Loading with Lumped Capacitors

One effective method for the miniaturization of SOLR filters is to add capacitive loading to the resonators via surface mount capacitors in series across the resonator gaps as shown in Figure 3.7 [37]. The area of the three pole filter in [37] loaded with 1 pF capacitors is only 20% that of a conventional SOLR filter without capacitive loading. The capacitive loading also improves the stopband performance by shifting the spurious resonances further away in frequency from the main resonance.

The resonators decrease in size as the capacitor values increase. If the resonator becomes too small, it is hard or impossible to achieve the required external quality factor by the tapping method shown in Figure 3.3. Also, as the capacitors become larger and the resonators smaller, the resonators need to be spaced closer together to achieve the proper coupling. These two effects establish an upper limit on the capacitor values used. For example, the capacitors used in the filters in Chapter 4 did not exceed 0.7 pF.
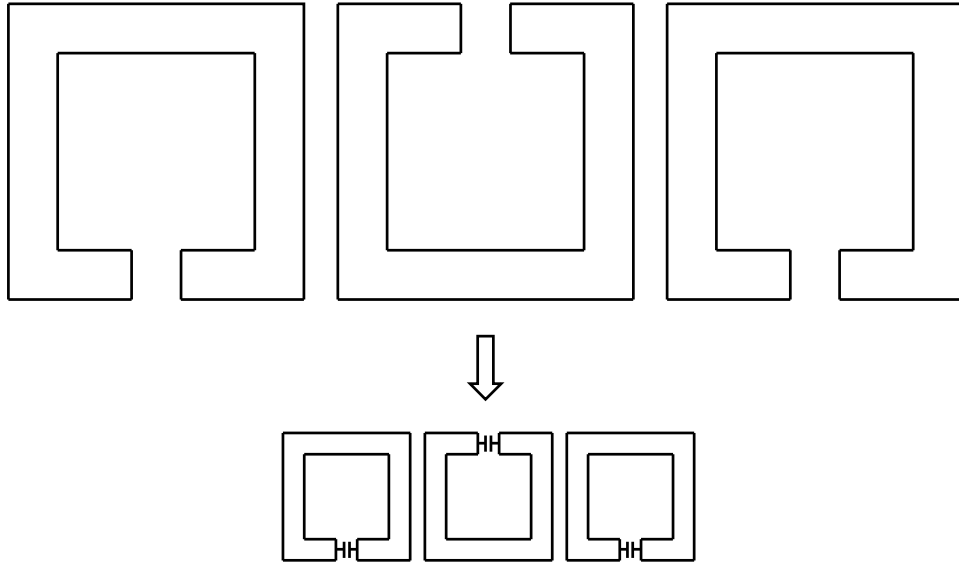
Figure 3.7 Conventional SOLR filter (top) miniaturized by capacitive loading via surface mount capacitors (bottom)

## Chapter 4: 3D Printed Square Open Loop Resonator (SOLR) Bandpass Filters[2]

### 4.1 Introduction

Miniaturized square open loop resonator (SOLR) bandpass filters are often used in communications due to their compact size [44]. SOLR filters have been miniaturized to an area of 20% that of a conventional SOLR filter by loading the resonators with surface mount capacitors [37]. For this study, square open loop resonator (SOLR) bandpass filters loaded with series capacitors were fabricated using additive manufacturing techniques, which has not been done before.

In this chapter, two 2.45 GHz bandpass filter designs are examined. The first filter design is a planar SOLR bandpass filter that is similar to one that could be fabricated on printed circuit board. The planar filters, termed Filters 1-3, are detailed in Section 4.2. Filter 2, the best performing fully printed planar filter, has an insertion loss of 4.1 dB and a 3 dB bandwidth of 230 MHz. Significant content from Section 4.2 has been previously published in a conference paper [45].

The second filter design, detailed in Section 4.3, is a 3D design that is compatible with 3D printing. The second filter, termed as Filter 4, is an SOLR filter that contains 3D capacitive plates used to couple the resonators together. Filter 4 has an insertion loss of 3.8 dB and a 3 dB bandwidth of 250 MHz.

---

[2] Portions of this chapter were previously published in [45]. Permission is included in Appendix A.

## 4.2 Printed Planar SOLR Filter

A planar bandpass SOLR filter was designed and printed on different substrates. A total of 3 filters were printed with CB028 thick film Ag paste deposited using the nScrypt printer. Filters 1-3 are shown in Figure 4.1. $S_{11}$ and $S_{21}$ of each filter can be seen in Figures 4.2-4.4. The filter dimensions are displayed in Figure 4.5. The filters were designed to operate at 2.45 GHz. The resonators are loaded with 0.5 pF capacitors for miniaturization. Each filter is printed on a different 32 mil substrate. Filters 1 and 2 are printed on 3D printed ABS substrates and Filter 3 is printed on 32 mil Rogers 4003c. All of the substrates differ in surface roughness – Filter 1 has the roughest substrate while Filter 3 has the smoothest. The substrate for Filter 1 has an average roughness Ra, of 10.4 μm, Filter 2 - 6.85 μm, and Filter 3 - 1.3 μm. As seen in Figures 4.2-4.4, the pass-band insertion loss of each filter decreases as the substrates become smoother. The 3dB bandwidth of Filter 1 is 180 MHz, Filter 2 – 230 MHz, Filter 3 – 210 MHz. The printing time was approximately 31 minutes - 30 minutes for the ABS substrates and 1 minute for the silver ink.

Full wave EM simulation of the filters without the capacitors was performed in HFSS. Ports were placed at the capacitor pads and a data set was generated. The data set was used in ADS for co-simulation with Modelithics full parasitic capacitor models. For the ABS substrates, a dielectric constant of 2.58 and a loss tangent of 0.0078 were used. For the Rogers 4003c substrate, a dielectric constant of 3.55 and a loss tangent of 0.0027 were used. The measured responses of Filters 1-3 are shifted upwards in frequency from 2.45 GHz. This can be explained by the 10% tolerance value of the capacitors. The simulations match the measured data when the capacitor values are lowered to 0.45 pF.
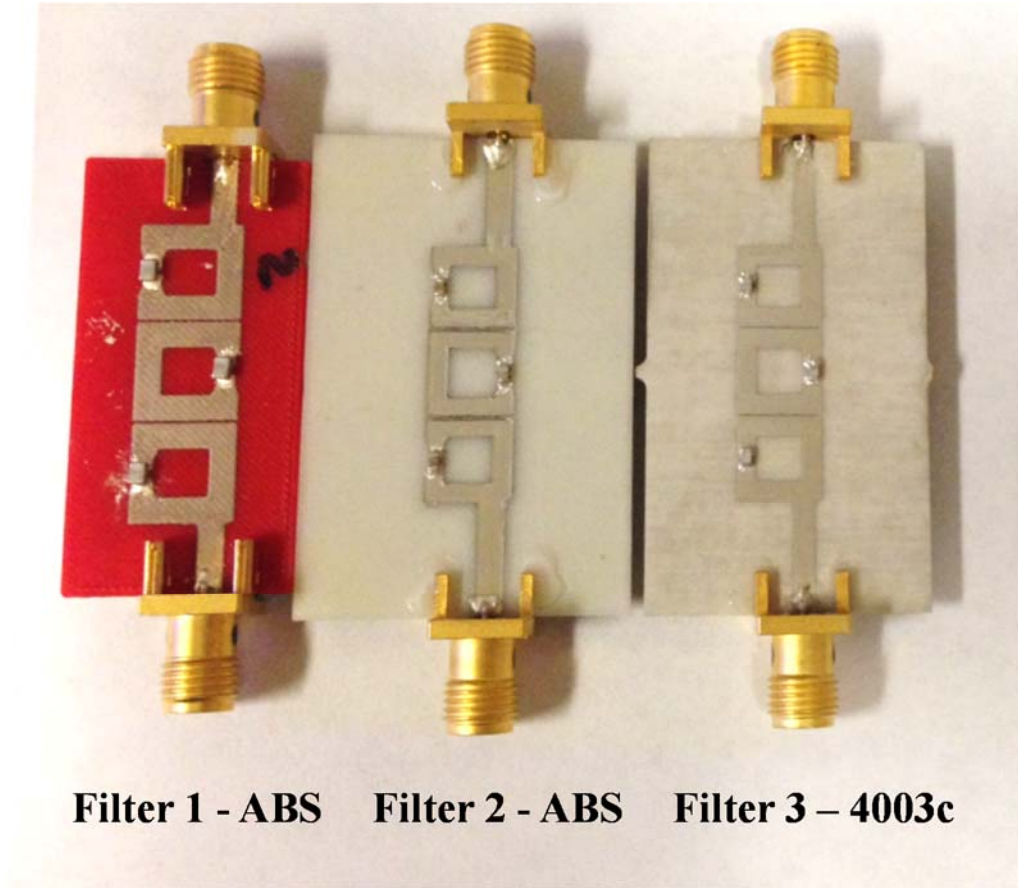
Figure 4.1 Filters 1-3: 3D printed planar bandpass filters. © 2015 IEEE
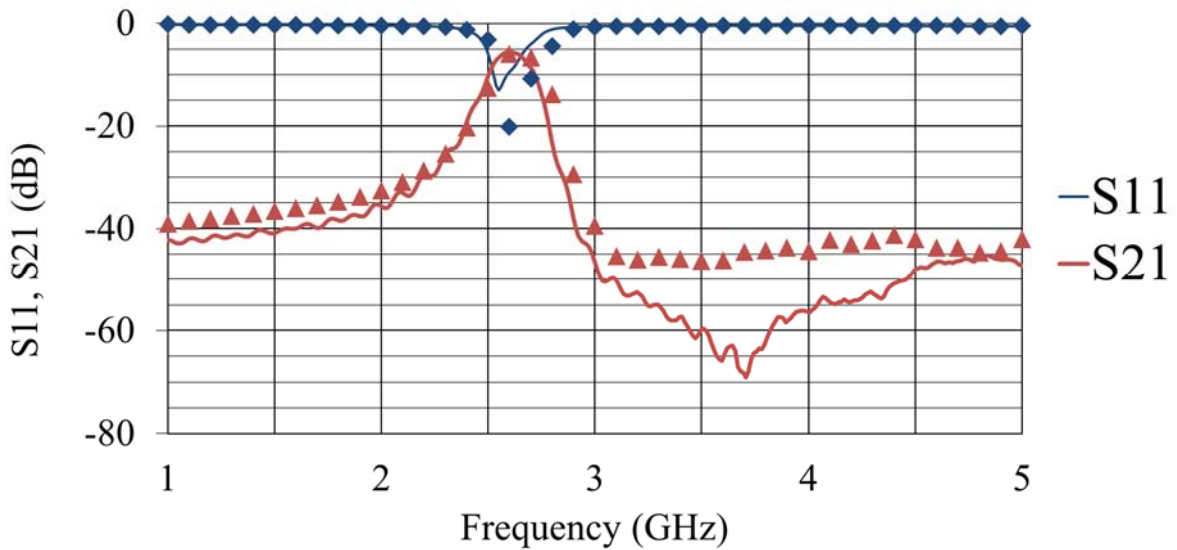


Figure 4.2 $S_{11}$ and $S_{21}$ of Filter 1. Simulated data represented by markers. © 2015 IEEE

28
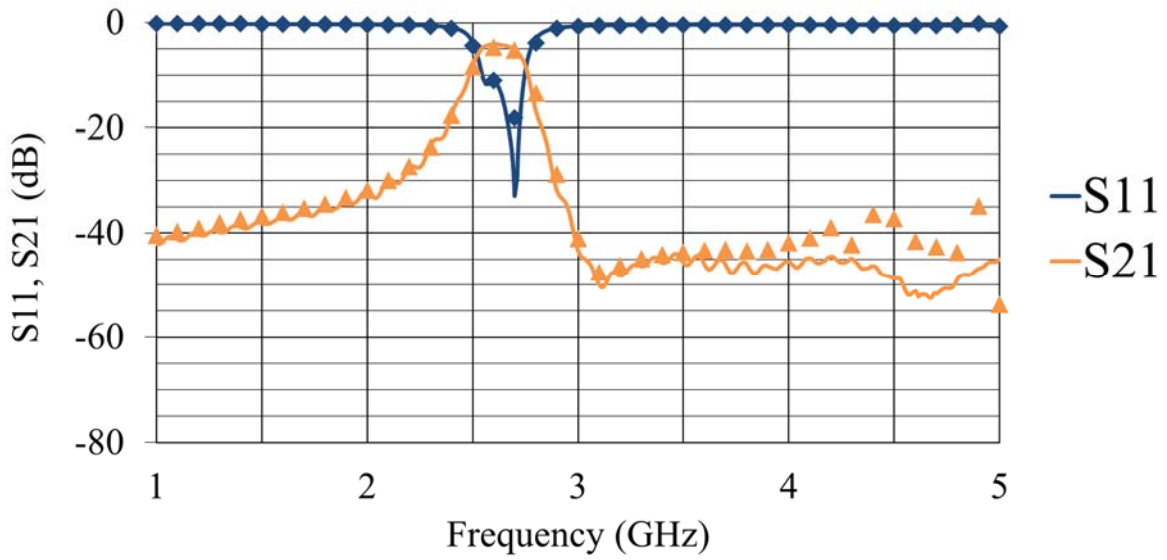
Figure 4.3 $S_{11}$ and $S_{21}$ of Filter 2. Simulated data represented by markers. © 2015 IEEE
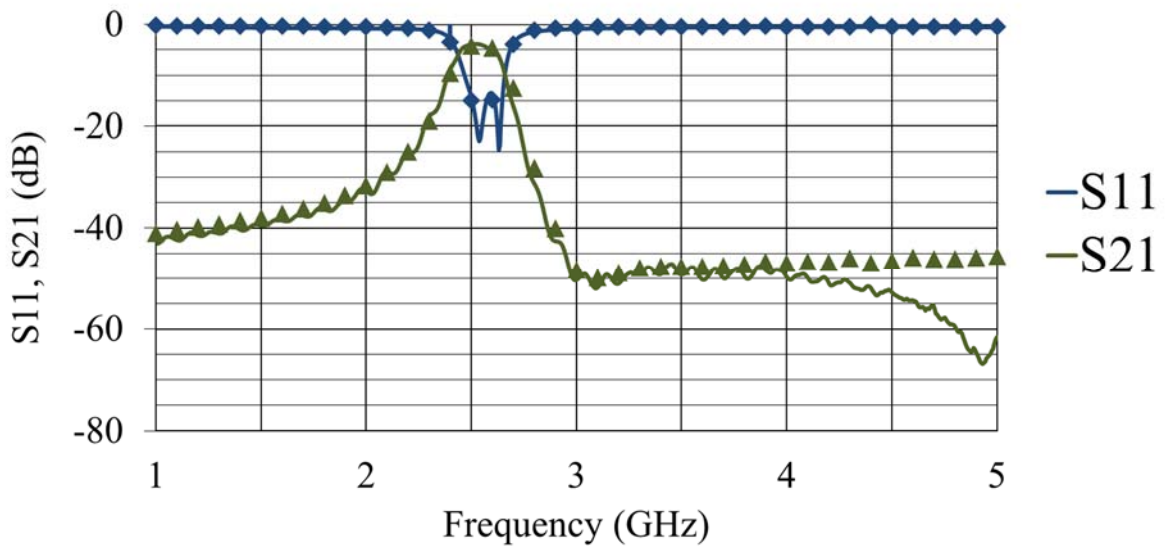


Figure 4.4 $S_{11}$ and $S_{21}$ of Filter 3. Simulated data represented by markers. © 2015 IEEE
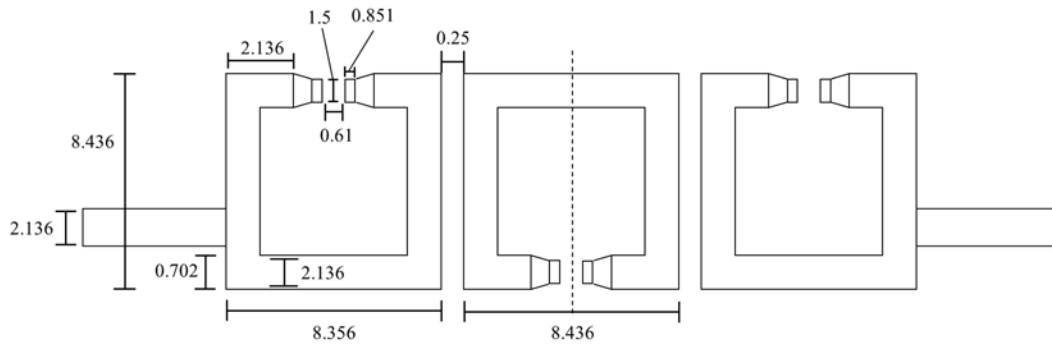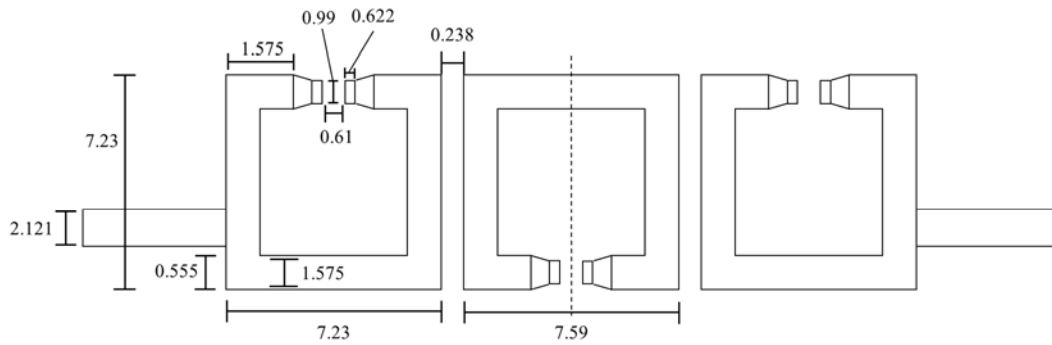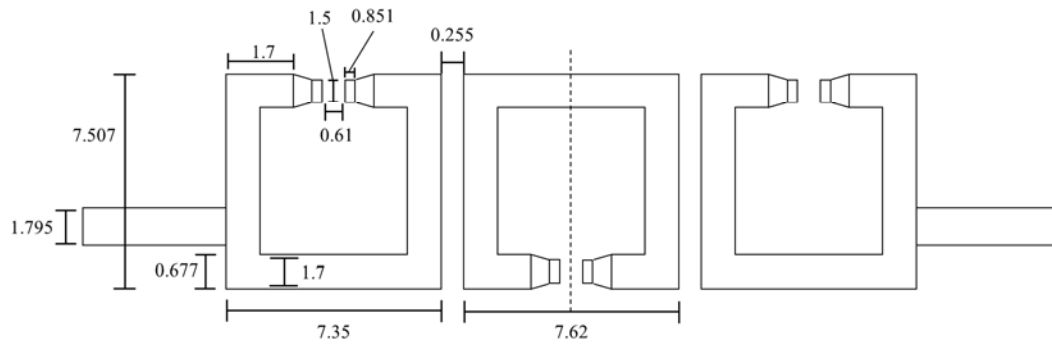
Figure 4.5 Dimensions for Filters 1-3. Filters are symmetrical across vertical dashed line. All units in mm.

A cross section of Filter 2 can be seen in Figure 4.6. The surfaces of the FDM printed substrates (Filters 1 and 2) are rough due to 50-100 µm valleys that run diagonally across the surface. A surface roughness measurement of a printed ABS substrate is shown in Figure 4.7 displaying the valleys.  These valleys result from the plastic being deposited line by line during

FDM printing. The substrate for Filter 2 has smaller valleys than Filter 1 because a higher resolution printer was used. When printing CB028 onto 3D printed substrates, the ink seeps into the valleys created. As a result, in a microstrip circuit, current concentrates in the valleys instead of the bulk of the transmission line above leading to a lower effective conductivity.
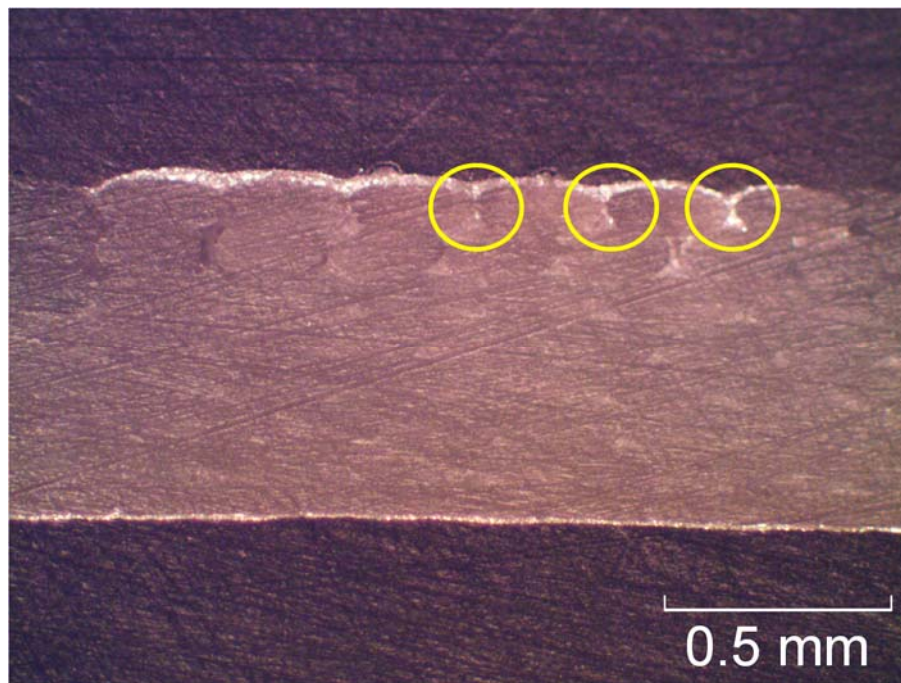


Figure 4.6 Cross section of Filter 2 demonstrating ink valleys. © 2015 IEEE
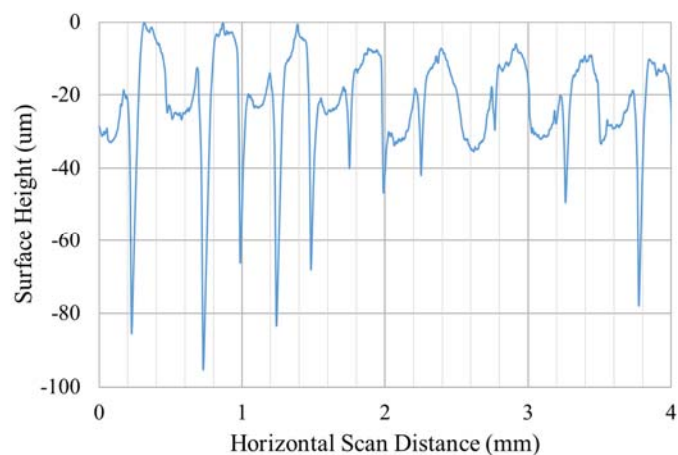


Figure 4.7 Surface roughness of FDM printed ABS substrate

31

Effective conductivity values that take into account surface roughness for CB028 lines printed on the different substrates were obtained indirectly via simulation. The conductivity values were varied in simulation to produce $S_{21}$ plots that match the measured responses, as shown in Figures 4.2-4.4. The values for RF conductivity obtained indirectly through simulations are shown in Table 4.1. From Table 4.1, the RF conductivity of printed CB028 ink and passband insertion loss can be seen as a function of surface roughness.

Table 4.1 Effective conductivity vs surface roughness for Filters 1-3

| Filter | Insertion Loss (dB) | Substrate $R_a$ (μm) | Effective Conductivity (S/m) |
|---|---|---|---|
| 1 | 5.5 | 10.4 | $0.60 \times 10^6$ |
| 2 | 4.1 | 6.85 | $0.90 \times 10^6$ |
| 3 | 3.8 | 1.3 | $1.15 \times 10^6$ |

## 4.3 Printed SOLR Filter with 3D Capacitive Plates

### 4.3.1 Resonator Coupling via 3D Capacitive Plates

As the resonators are loaded with larger capacitors, they become smaller. The smaller the resonator, the closer they need to be spaced in order to achieve the same coupling coefficient, k, because there is less line length available for each resonator for coupling to an adjacent resonator. In this work, given the roughness of the ABS substrates, the aim was to avoid gap sizes less than 100 μm so that the lines would not bleed together during printing. Additional coupling methods have to be used when a gap less than 100 μm is required to achieve sufficient coupling. More coupling between the resonators can be attained with a capacitive plate like the one shown in Figure 4.8a.

In Figure 4.8a, two resonators loaded with capacitors are coupled together by a 3D capacitive plate. The resonators are separated by a gap of g. The capacitive plate has a width of *w*

and is sitting on an ABS dielectric of thickness $t$. The coupling coefficient, k, between the resonators was calculated for different values of $t$ and $w$ via full wave EM simulation and co-simulation with full parasitic capacitor models. For the simulation, $g = 500$ μm and the resonators are loaded with 0.7 pF capacitors. At $w = 0$ (see Figure 4.8b), there is no capacitive plate, which is why all the traces converge to a single point. At $w = g$, the plate is the same width as the gap, as shown in Figure 4.8b. For $w > g$ μm, the plate is overlapping the resonators. A plot of k vs. $t$ and $w$ is shown in Figure 4.8c. The coupling coefficient increases as the width of the capacitive plate increases. Also, stronger coupling occurs when the dielectric thickness, $t$, is smaller.
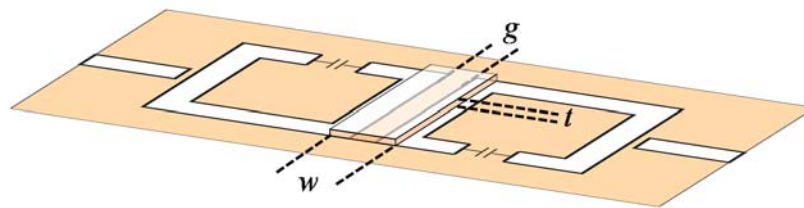


Figure 4.8a Resonators spaced by a gap, $g$, coupled with capacitive plate of width, $w$ and thickness, $t$
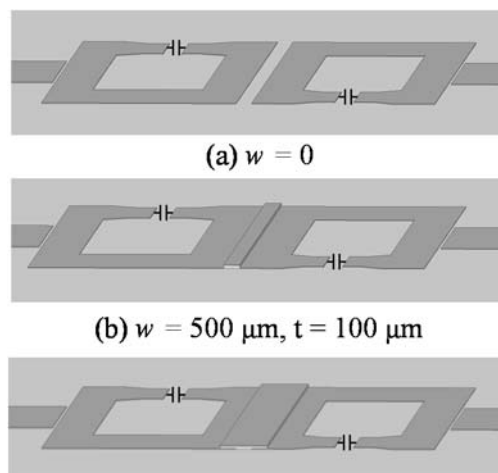


Figure 4.8b Extreme widths of capacitive plate. a) $w = 0$ (no plate) and b) $w = g = 500$ μm c) $w = 1500$ μm
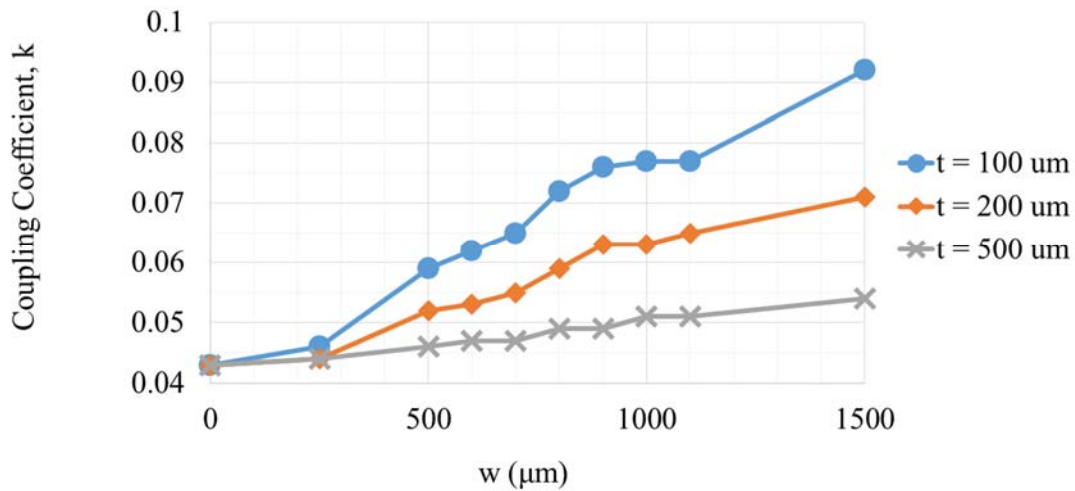
Figure 4.8c Coupling coefficient, k vs. capacitive plate width, *w* and thickness, *t*

### 4.3.2 Printed Filter Design and Results

Filter 4 is a 3D bandpass SOLR filter that was designed and printed with CB028 ink on printed ABS. Filter 4 is shown in Figure 4.9. $S_{11}$ and $S_{21}$ measurements are displayed in Figure 4.10. Simulated data is represented by markers. The dimensions of the filter are displayed in Figure 4.12. The filter has a 3 dB bandwidth of 250 MHz and a pass band insertion loss of 3.8 dB. The resonators are loaded with 0603 0.7 pF capacitors for miniaturization. The total area of the filter is 1.08 cm$^2$. The filter was designed for 2.45 GHz but the measured resonance is at 2.35 GHz. This can be explained because a 5% tolerance was expected with the capacitors for the design, i.e. the filter was actually designed for 0.65 pF capacitors. It is now assumed that the capacitors are actually 0.7 pF because the simulation matches the measurement when the capacitors are set to 0.7 pF. Filter 4 is printed on a 32mil ABS substrate with a surface roughness of 6.85 μm, like the substrate used for Filter 2 in Section 4.1. Likewise, the conductivity value of 0.90 x 10$^6$ S/m was used in simulation to achieve good matching with the measured data. The gaps between the resonators were required to be approximately 70 μm to achieve the proper

34

coupling coefficient, k = 0.05. To avoid having to print a 70 μm gap, capacitive plates were implemented and the gap was set to 500 μm (see Figure 4.13). The overlap area between one of the capacitive plates and a single resonator is 6.3 mm$^2$ with a 0.4 mm thick layer of ABS ($\epsilon_r$ = 3.58) in between. These numbers plugged into the parallel plate capacitor equation yields a capacitance of 0.5 pF between each resonator arm and its 3D capacitive plate. For comparison, Figure 4.11 displays the simulated S21 responses of Filter 4 with and without capacitive plates. The filter without capacitive plates achieves the proper coupling by a gap of 70 μm between the resonators. The out of band return loss is approximately 5 dB higher for the filter with the capacitive plates.

The printing time was approximately 34 minutes - 30 minutes for the ABS substrate, 1 minute for the silver ink of the filter, 2 minutes for the ABS dielectric of the capacitive plates, and 1 minute for the silver ink of the capacitive plates.
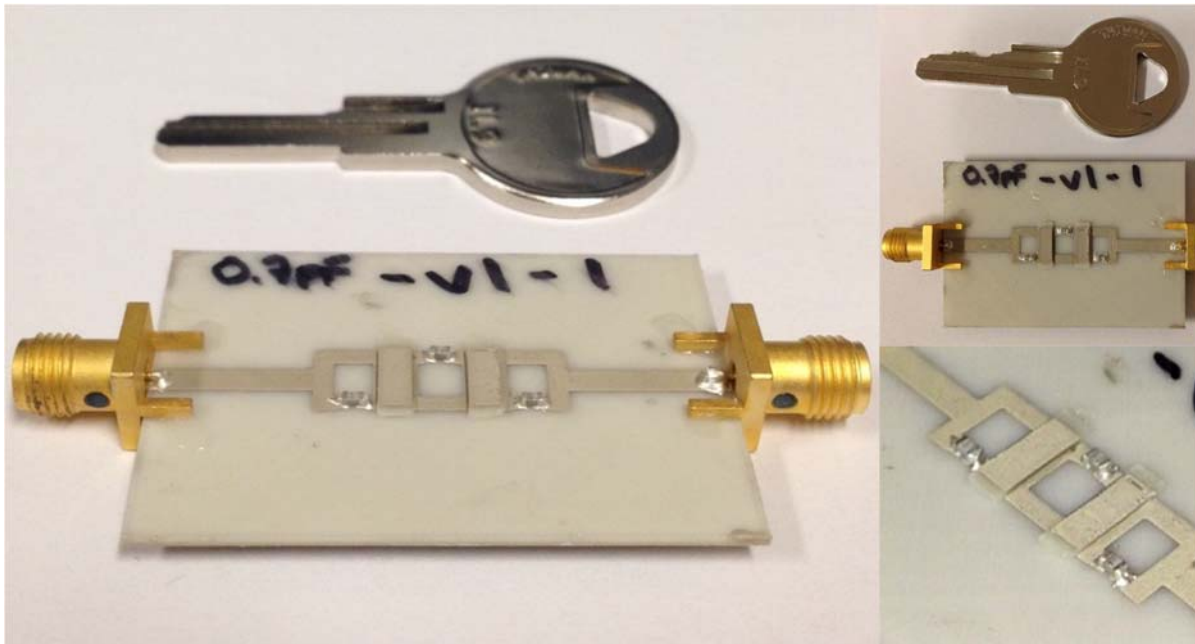


Figure 4.9 Filter 4: 3D printed filter with 3D capacitive plates
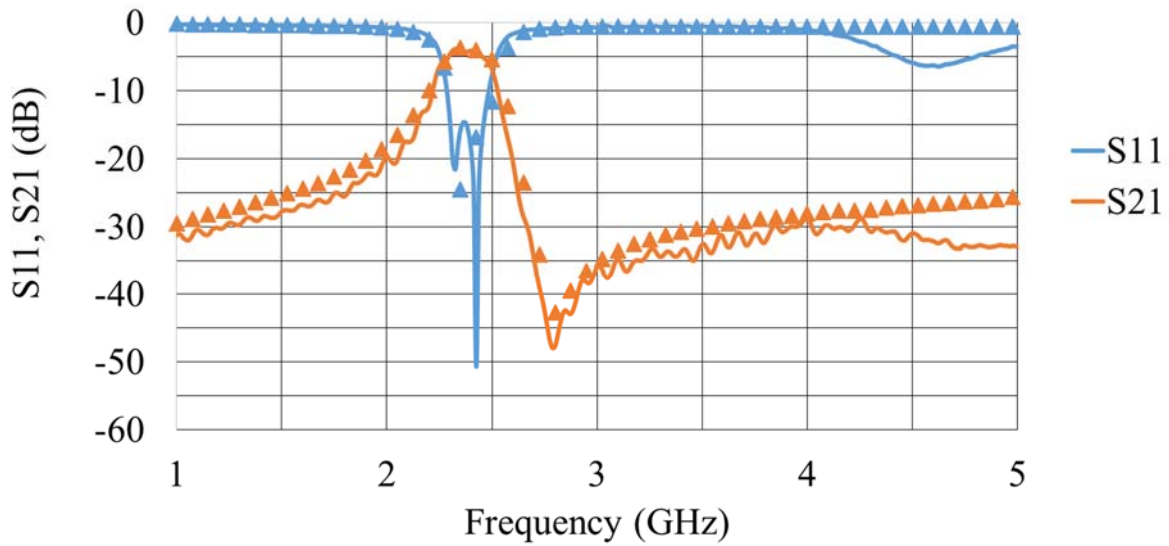
Figure 4.10 $S_{11}$ and $S_{21}$ of Filter 4. Simulated data represented by markers.
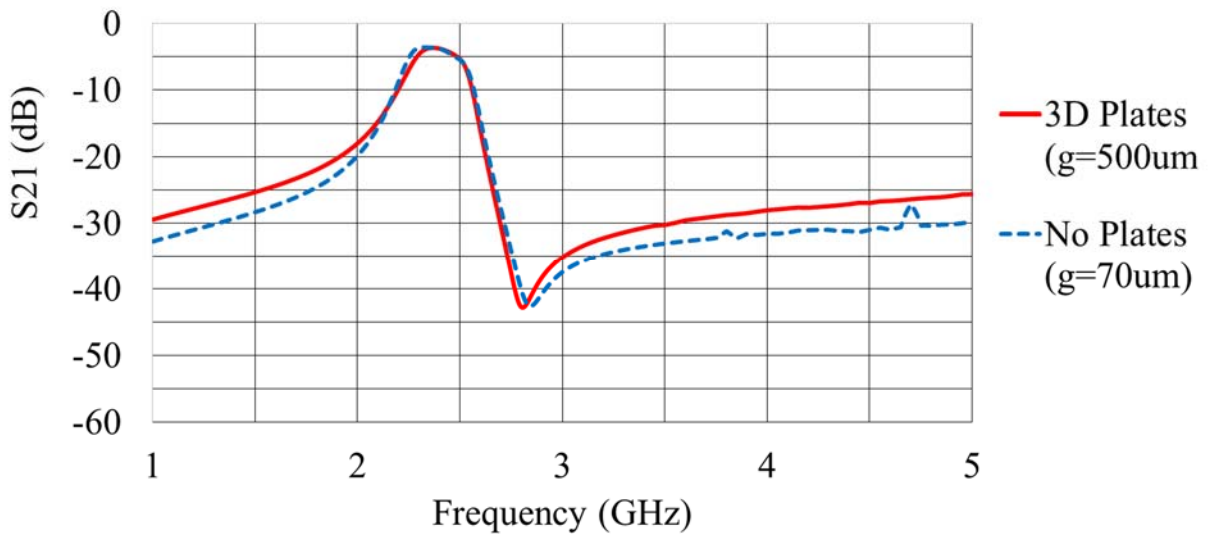


Figure 4.11 Simulated $S_{21}$ of Filter 4 with 3D capacitive plates (g = 500um) and without 3D capacitive plates (g = 70um)

36
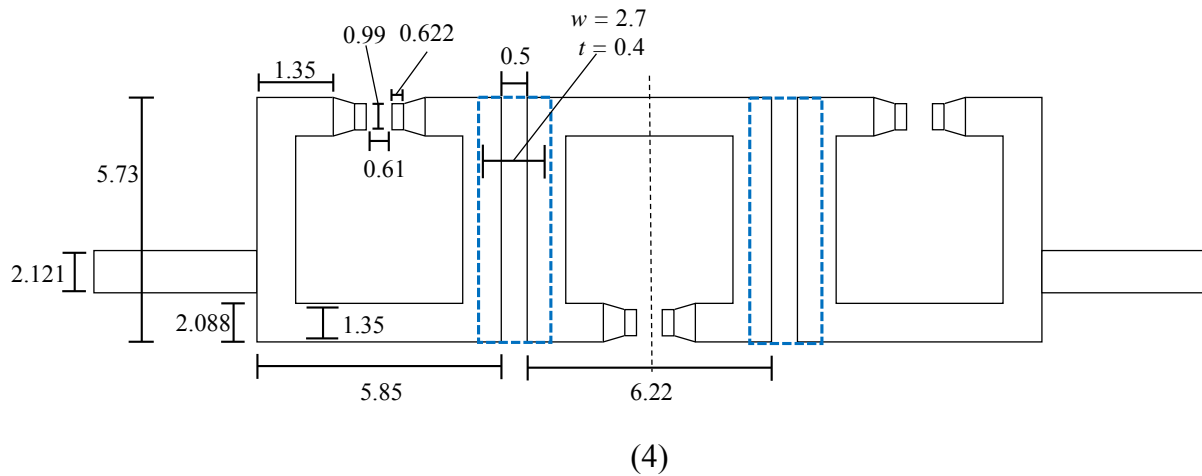
Figure 4.12 Dimensions for Filter 4. Filter is symmetrical across vertical dashed line. Overlapping capacitive plate of thickness *t* and width *w* shown by dashed blue line. All units in mm.
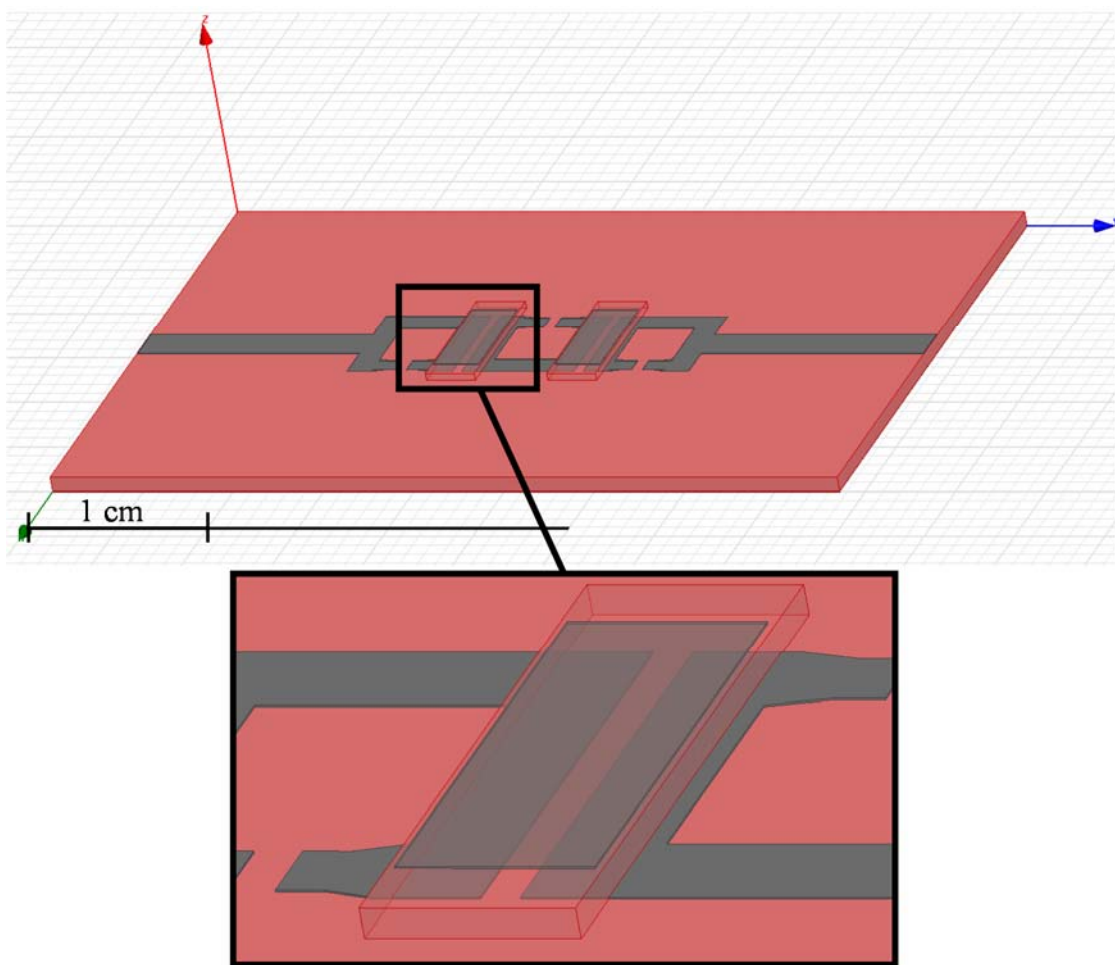


Figure 4.13 3D printed capacitive plates across coupled resonators

37

## 4.4 Conclusion

Table 4.2 summarizes the key parameters of Filters 1-4. For performance comparison, a planar PCB filter, similar to Filter 1, was designed on Rogers 4003c with ½ ounce copper. The filter, shown in Figure 4.14, has an insertion loss of 1.5 dB. Figure 4.15 compares $S_{21}$ of Filters 1-4 with the PCB filter design on Rogers. Each trace has been centered to be at 2.45GHz for comparison.

For size comparison, a conventional, unloaded SOLR 2.45 GHz filter was simulated in ADS. The total area of the conventional filter is 5.11 cm$^2$. The substrate for the conventional filter is ABS with $R_a$ = 6.85 μm and the conductor is CB028 with a conductivity of 0.9 x 10$^6$ S/m. A comparison of the footprints of Filters 1-4 and the conventional, unloaded SOLR filter can be seen in Figure 4.16.

In conclusion, additive manufacturing has been shown to be a feasible process for manufacturing SOLR bandpass filters. The surface roughness of a substrate has been shown to be related to conductivity when conductive ink is printed via DPAM. In addition, additive manufacturing has been shown to allow for 3 dimensional design features that would be impossible with printed circuit board, like the novel 3D capacitive plates demonstrated in Filter 4.

Table 4.2 Comparison of Filters 1-4

| Filter | Substrate | Capacitor Value (pF) | Total Area (cm$^2$) | Insertion Loss (dB) | Substrate Roughness, $R_a$ (μm) | 3-dB Bandwidth (MHz) | % Area vs conventional SOLR filter |
|---|---|---|---|---|---|---|---|
| 1 | ABS | 0.5 | 2.24 | 5.5 | 10.4 | 180 | 43.4 |
| 2 | ABS | 0.5 | 1.62 | 4.1 | 6.85 | 230 | 31.7 |
| 3 | Rogers 4003c | 0.5 | 1.71 | 3.8 | 1.3 | 210 | 33.5 |
| 4 | ABS | 0.7 | 1.08 | 3.8 | 6.85 | 250 | 21.1 |

Figure 4.14 Planar SOLR filter, similar to Filter 1, designed on Rogers 4003 with ½ ounce copper
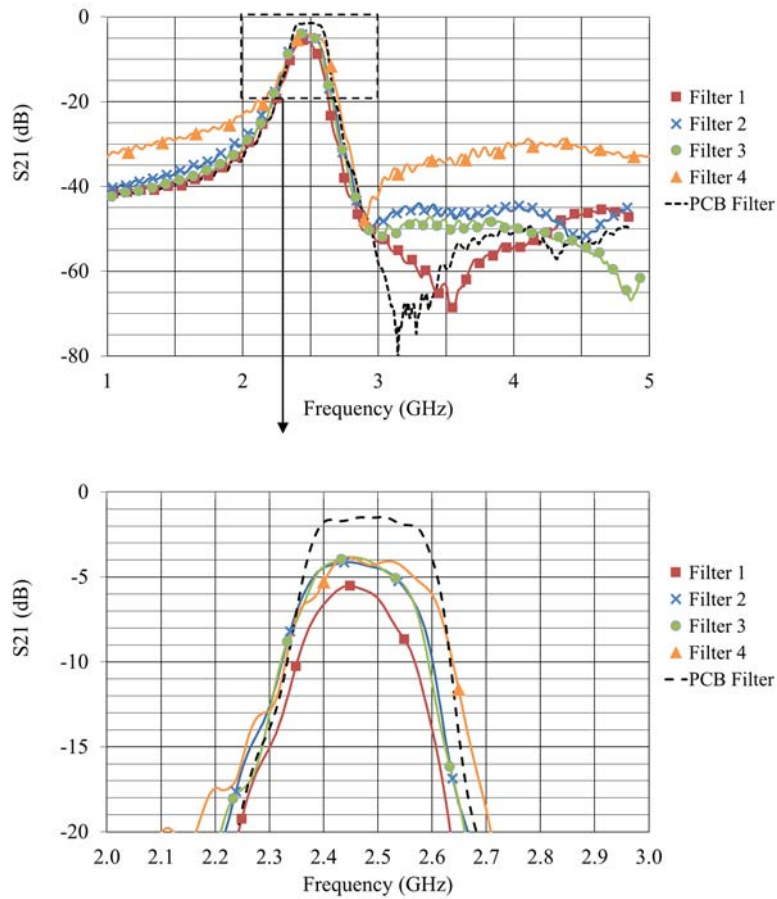


Figure 4.15 Measured $S_{21}$ of Filters 1-4 centered at 2.45 GHz for comparison
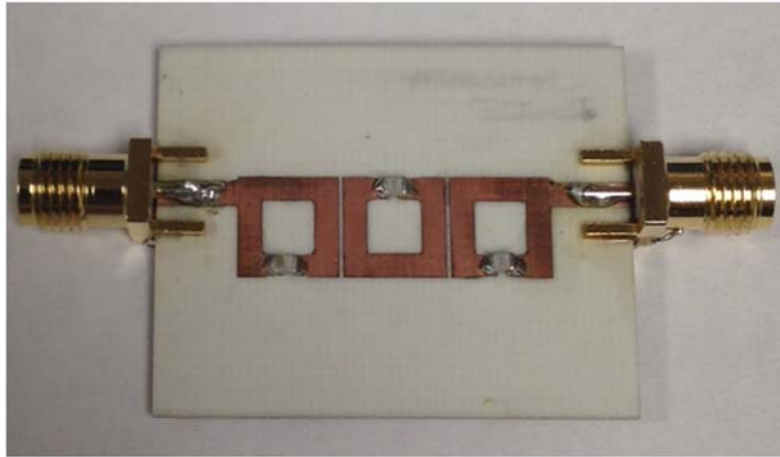
39

Conventional – 5.11 cm²
ABS, Unloaded

Filter 1 - 2.24 cm²
ABS, C= 0.5 pF

Filter 2 – 1.62 cm²
ABS, C= 0.5 pF

Filter 3 – 1.71 cm²
Rogers, C= 0.5 pF

Filter 4 – 1.08 cm²
ABS, C= 0.7 pF
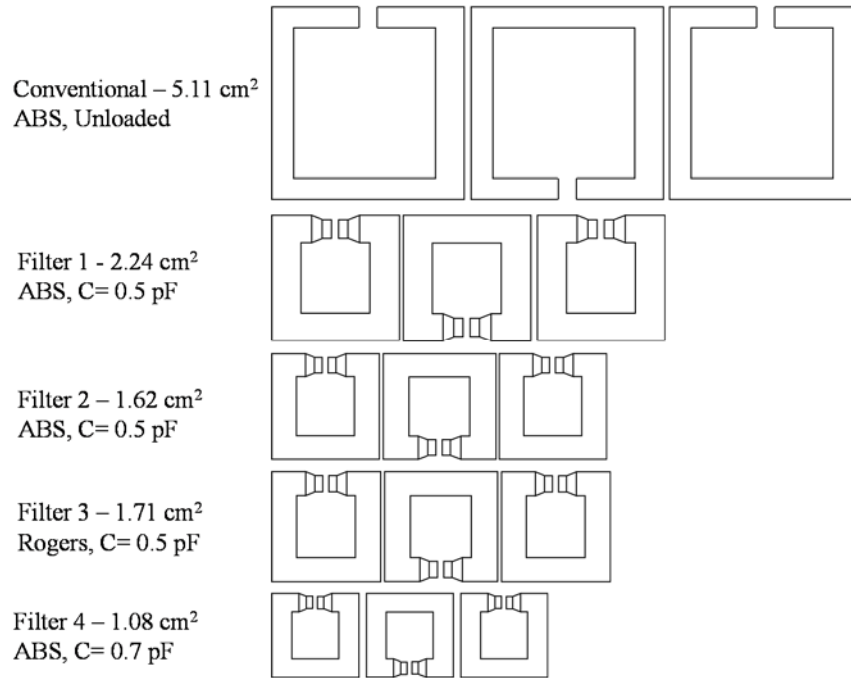
Figure 4.16 Footprints of Filters 1-4 (to scale)

**Chapter 5: Conclusion**

The use of additive manufacturing techniques for the fabrication of microwave circuitry is valuable because of the opportunity to design and miniaturize in 3 dimensions. Also, it allows for the possibility to embed electronics in a structure or to conform electronics to a curved surface. The work in this thesis demonstrates that additive manufacturing is a viable method for bandpass filter fabrication. The insertion losses of the 3D printed filters in this thesis were only 3 dB less than the same filters on low loss microwave laminate (Rogers 4003, $\epsilon_r$ = 3.55, tan δ = 0.0027) - the primary reason for this is the lower conductivity of printed conductors. All the more, it was shown that additive manufacturing encourages innovative 3D design, as in the case of the SOLR filter coupled together with 3D capacitive plates. Appendix A demonstrates that additive manufacturing is a possible option for replicating commercial antenna handsets. Finally, the work in this thesis shows that substrate surface roughness leads to a lower effective conductivity for printed conductors.

**5.1 Recommendations**

Further areas of study include:

1. The filters can be fully 3D printed and without lumped components if the capacitors loading the resonators in Filters 1-4 are replaced with 3D printed capacitors.

2.  The filter designed in Section 4.2 could be further miniaturized with a folding technique like the one shown in Figure 1.1. Also, the resonators may be able to be coupled together with a stacking method as shown in Figure 5.2.

3.  Improvements to the conductivities of the printed conductors will improve the performance of the filters in this thesis.
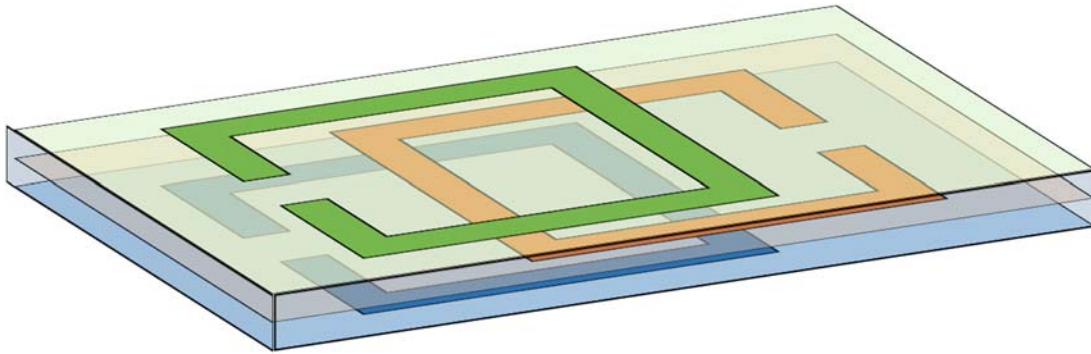


Figure 5.1 Possible 3D miniaturization of SOLR filter by stacking resonators

# References

[1]     B. Hale, 'The Best 3D Printers for 2015', 11-Jan-2015. [Online]. Available: http://3dforged.com/best-3d-printers/. [Accessed: 18-Feb-2015].

[2]     L. Gilpin, '3D printing: 10 companies using it in ground-breaking ways', 26-Mar-2014. [Online]. Available: http://www.techrepublic.com/article/3d-printing-10-companies-using-it-in-ground-breaking-ways/. [Accessed: 02-Apr-2015].

[3]     J. Koebler, '3-D Printed Medical Device Saves a Life for the First Time', 22-May-2013. [Online]. Available: http://www.usnews.com/news/articles/2013/05/22/3-d-printed-medical-device-saves-a-life-for-the-first-time. [Accessed: 02-Apr-2015].

[4]     'Layer by Layer | MIT Technology Review', 19-Dec-2011. [Online]. Available: http://www.technologyreview.com/featuredstory/426391/layer-by-layer/. [Accessed: 18-Feb-2015].

[5]     G. Wable and D. Gamota, 'An Update on Manufacturing with Additive Processes', in *Surface Mount Technology Association International*, 2014.

[6]     I. Nassar,  T. Weller, and  H. Tsang, '3D printed wideband harmonic transceiver for embedded passive wireless monitoring', *Electronics Letters*, vol. 50, no. 22, pp. 1609–1611, 2014.

[7]     E. Macdonald, R. Salas, D. Espalin, M. Perez, E. Aguilera, D. Muse, and R. B. Wicker, '3D Printing for the Rapid Prototyping of Structural Electronics', *IEEE Access*, vol. 2, pp. 234–242, 2014.

[8]     A. J. Lopes, E. MacDonald, and R. B. Wicker, 'Integrating stereolithography and direct print technologies for 3D structural electronics fabrication', *Rapid Prototyping Journal*, vol. 18, no. 2, pp. 129–143, 2012.

[9]     K. Perez and C. Williams, 'Combining Additive Manufacturing and Direct Write for Integrated Electronics – A Review', in *Solid Freeform Fabrication Symposium*, 2013, pp. 962–979.

[10]    D. Manessis et al. 'Large-scale manufacturing of embedded subsystems-in-substrates and a 3D-stacking approach for a miniaturised medical system integration', in *EMPC*, Grenbole, FR, 2013.

[11] P. Salonen et al. '211.1: Direct Printing Of A Handset Antenna On A 3D Surface.', in *IEEE Antennas And Propagation Society International Symposium*, 2013.

[12] M. Mäntysalo and P. Mansikkamäki, 'An inkjet-deposited antenna for 2.4 GHz applications', *AEU - International Journal of Electronics and Communications*, vol. 63, no. 1, pp. 31–35, 2009.

[13] S. Koskinen, L. Pykari, and M. Mantysalo, 'Electrical Performance Characterization of an Inkjet-Printed Flexible Circuit in a Mobile Application', *IEEE Transactions on Components, Packaging and Manufacturing Technology*, vol. 3, no. 9, pp. 1604–1610, 2013.

[14] J. J. Adams, E. B. Duoss, T. F. Malkowski, M. J. Motala, B. Y. Ahn, R. G. Nuzzo, J. T. Bernhard, and J. A. Lewis, 'Conformal Printing of Electrically Small Antennas on Three-Dimensional Surfaces', *Advanced Materials*, vol. 23, no. 11, pp. 1335–1340, 2011.

[15] H. Subbaraman, D. T. Pham, X. Xu, M. Y. Chen, A. Hosseini, X. Lu, and R. T. Chen, 'Inkjet-Printed Two-Dimensional Phased-Array Antenna on a Flexible Substrate', *IEEE Antennas and Wireless Propagation Letters*, vol. 12, pp. 170–173, 2013.

[16] B. Cook and M. Tentzeris, '301.2 A Miniaturized Wearable High Gain and Wideband Inkjet-printed AMC Antenna', in *IEEE Antennas And Propagation Society International Symposium*, 2013.

[17] J. O'Brien et al. 'A Switched-Line Microwave Phase Shifter Fabricated with Additive Manufacturing', in *IMAPS Symposium*, 2013.

[18] U. Rodriguez, '3D Printed Impedance Elements By Micro-dispensing', Thesis, UTEP, El Paso, TX, 2013.

[19] D. Williams et al. 'Aerosol Deposition of Integrated Capacitors', in *IMAPS Symposium*, 2007.

[20] F. Cai et al. 'Aerosol Jet Printing for 3-D Multilayer Passive Microwave Circuitry', in *European Microwave Conference (EuMC)*, 2014.

[21] I. Gibson, D. W. Rosen, and B. Stucker, *Additive manufacturing technologies rapid prototyping to direct digital manufacturing*. New York: Springer, 2010.

[22] 'Fortus 360mc 400mc 3D Prototyping Machine', *Stratasys*. [Online]. Available: http://www.stratasys.com/3d-printers/production-series/fortus-360-400mc. [Accessed: 02-Feb-2015].

[23]   M. D. Monzón, I. Gibson, A. N. Benítez, L. Lorenzo, P. M. Hernández, and M. D. Marrero, 'Process and material behavior modeling for a new design of micro-additive fused deposition', *The International Journal of Advanced Manufacturing Technology*, vol. 67, no. 9–12, pp. 2717–2726, Aug. 2013.

[24]   'Stratasys Launches Six PolyJet 3D Printers', *CAD/CAM Update*, vol. 26, no. 12. pp. 4–6.

[25]   'PolyJet Technology'. [Online]. Available: http://www.stratasys.com/3d-printers/technologies/polyjet-technology. [Accessed: 02-Feb-2015].

[26]   K. Kincade, 'Rapid prototyping evolves into custom manufacturing', *Laser Focus World*, vol. 41, no. 5, pp. 129–134, May-2005.

[27]   J. Liu, H. Hu, P. Li, C. Shuai, and S. Peng, 'Fabrication and Characterization of Porous 45S5 Glass Scaffolds via Direct Selective Laser Sintering', *Materials and Manufacturing Processes*, 2013.

[28]   'Micro Dispense Pump - Direct Print SmartPump Systems'. [Online]. Available: http://www.nscrypt.com/direct-print-smartpump/index.php. [Accessed: 02-Apr-2015].

[29]   C. Werner, D. Godlinski, V. Zöllmer, and M. Busse, 'Morphological influences on the electrical sintering process of Aerosol Jet and Ink Jet printed silver microstructures', *Journal of Materials Science: Materials in Electronics*, vol. 24, no. 11, pp. 4367–4377, Nov. 2013.

[30]   'Aerosol Jet Technology - Optomec Additive Manufacturing'.

[31]   D. Gries, 'Laser direct structuring creates low-cost 3D integrated circuits', *Laser Focus World*, vol. 46, no. 10, pp. 59–63, Oct-2010.

[32]   P. I. Deffenbaugh, R. C. Rumpf, and K. H. Church, 'Broadband Microwave Frequency Characterization of 3-D Printed Materials', *IEEE Transactions on Components, Packaging and Manufacturing Technology*, vol. 3, no. 12, pp. 2147–2155, 2013.

[33]   F. Cai et al. 'Aerosol jet printing for 3-D multilayer passive microwave circuitry', in *European Microwave Conference (EuMC)*, Rome, Italy, 2014, pp. 512–515.

[34]   'Thermal Treatment for Parts Made of Objet RGD5160-DM'. [Online]. Available: http://www.smg3d.co.uk/files/doc-08269_d_rgd5160-dm_thermal-treatment.pdf. [Accessed: 02-Feb-2015].

[35]   V. Marinov, 'Electrical Resistance of Laser Sintered Direct-Write Deposited Materials for Microelectronic Applications'. [Online]. Available: http://www.capres.com/Files/Filer/Valery_Marinov_CAPRES_rev2.pdf. [Accessed: 02-Feb-2015].
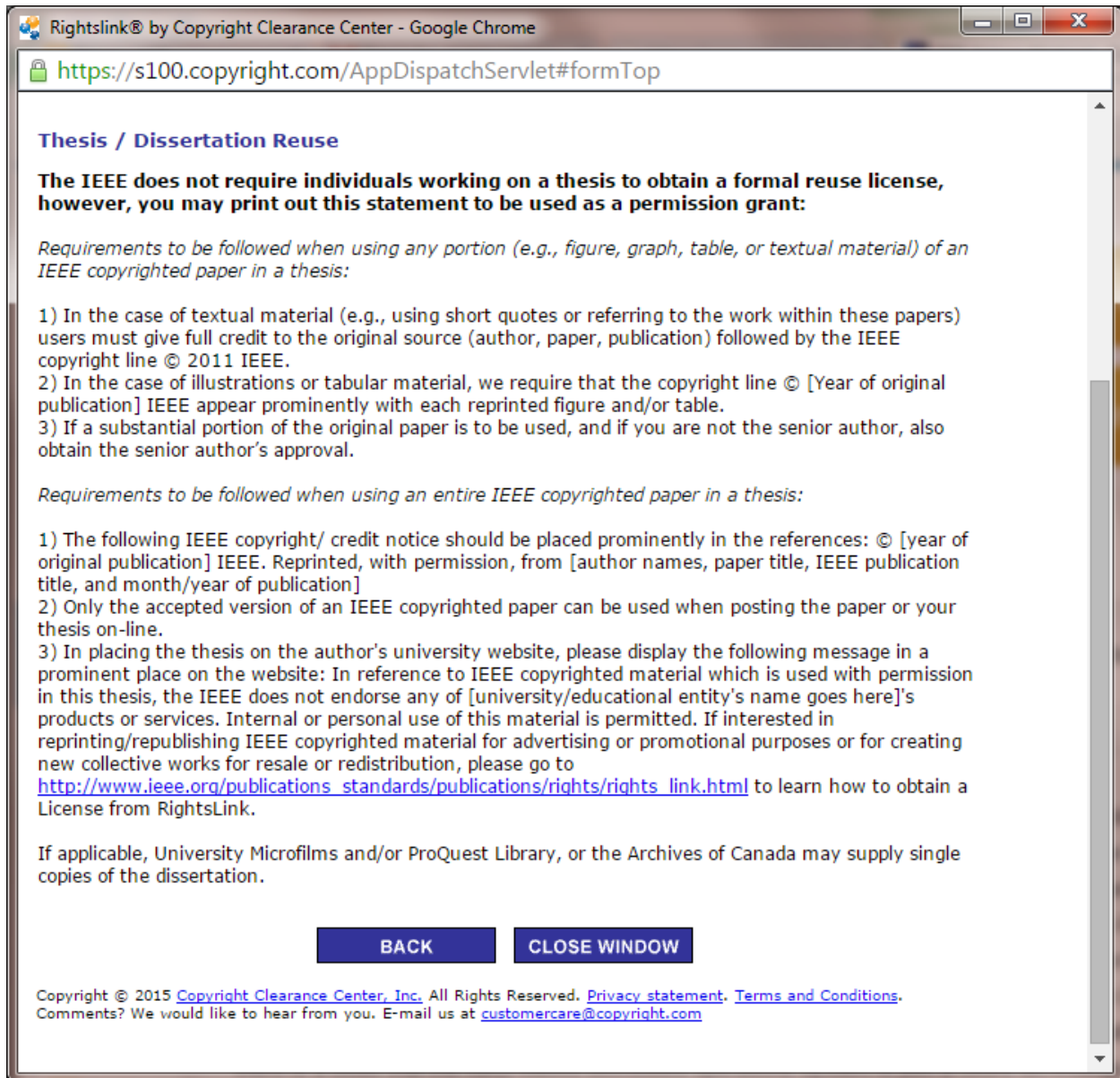
[36]     J. S. Hong and M. J. Lancaster, 'Compact microwave elliptic function filter using novel microstrip meander open-loop resonators', *Electronics Letters*, vol. 32, no. 6, 1996.

[37]     L. Ledezma and T. Weller, 'Miniaturization of Microstrip Square Open Loop Resonators Using Surface Mount Capacitors', in *Wireless and Microwave Technology Conference (WAMICON)*, 2011.

[38]     N. Kumar and Y. K. Singh, 'Compact stub-loaded open-loop BPF with enhanced stopband by introducing extra transmission zeros', *Electronics Letters*, 2015.

[39]     V. Soni and M. Kumar, 'New Kinds of Fractal Iterated and Miniaturized Narrowband Bandpass Filters for Wireless Applications', in *International Conference on Advances in Computing, Communications and Informatics (ICACCI)*, 2014.

[40]     J.S. Hong, H. Shaman, and Y.-H. Chun, 'Dual-Mode Microstrip Open-Loop Resonators and Filters', *IEEE Transactions on Microwave Theory and Techniques*, vol. 55, no. 8, pp. 1764–1770, 2007.

[41]     D. M. Pozar, *Microwave engineering*, 4th ed. New York, NY: John Wiley and Sons (WIE), 2011.

[42]     J.-S. Hong and M. J. Lancaster, *Microstrip Filters for RF/Microwave Applications*. New York, NY [u.a.]: Wiley-Interscience, 2001.

[43]     E. Belohoubek and  E. Denlinger, 'Loss Considerations for Microstrip Resonators (Short Papers)', *IEEE Transactions on Microwave Theory and Techniques*, vol. 23, no. 6, pp. 522–526, 1975.

[44]     J.-S. Hong and M. J. Lancaster, 'Couplings of microstrip square open-loop resonators for cross-coupled planar microwave filters', *IEEE Transactions on Microwave Theory and Techniques*, vol. 44, no. 11, pp. 2099–2109, 1996.

[45]     N. Arnal et al. '3D Multi-Layer Additive Manufacturing of a 2.45 GHz RF Front End', in *International Microwave Symposium (IMS)*, Phoenix, AZ, 2015.

[46]     N. Arnal et al. '3D Digital Manufacturing and Characterization of Antennas Integrated in Mobile Handset Covers', in *Wireless and Microwave Technology Conference (WAMICON)*, Cocoa Beach, FL, 2015.

**Appendices**

## Appendix A: Copyright Permissions

Below is permission for the use of Table 2.2, Figure 4.1, Figure 4.2, Figure 4.3, Figure 4.4, Figure 4.6, Figure A.8, material in Chapter 2, material in Chapter 4, and material in Appendix A.

**Rightslink® by Copyright Clearance Center - Google Chrome**

🔒 https://s100.copyright.com/AppDispatchServlet#formTop

### Thesis / Dissertation Reuse

**The IEEE does not require individuals working on a thesis to obtain a formal reuse license, however, you may print out this statement to be used as a permission grant:**

*Requirements to be followed when using any portion (e.g., figure, graph, table, or textual material) of an IEEE copyrighted paper in a thesis:*

1) In the case of textual material (e.g., using short quotes or referring to the work within these papers) users must give full credit to the original source (author, paper, publication) followed by the IEEE copyright line © 2011 IEEE.
2) In the case of illustrations or tabular material, we require that the copyright line © [Year of original publication] IEEE appear prominently with each reprinted figure and/or table.
3) If a substantial portion of the original paper is to be used, and if you are not the senior author, also obtain the senior author's approval.

*Requirements to be followed when using an entire IEEE copyrighted paper in a thesis:*

1) The following IEEE copyright/ credit notice should be placed prominently in the references: © [year of original publication] IEEE. Reprinted, with permission, from [author names, paper title, IEEE publication title, and month/year of publication]
2) Only the accepted version of an IEEE copyrighted paper can be used when posting the paper or your thesis on-line.
3) In placing the thesis on the author's university website, please display the following message in a prominent place on the website: In reference to IEEE copyrighted material which is used with permission in this thesis, the IEEE does not endorse any of [university/educational entity's name goes here]'s products or services. Internal or personal use of this material is permitted. If interested in reprinting/republishing IEEE copyrighted material for advertising or promotional purposes or for creating new collective works for resale or redistribution, please go to http://www.ieee.org/publications_standards/publications/rights/rights_link.html to learn how to obtain a License from RightsLink.

If applicable, University Microfilms and/or ProQuest Library, or the Archives of Canada may supply single copies of the dissertation.

BACK    CLOSE WINDOW